

RECONSTRUCTING RELAXED CONFIGURATIONS IN ELASTIC BODIES: MATHEMATICAL FORMULATION AND NUMERICAL METHODS FOR CARDIAC MODELING

N. A. BARNAFI¹, F. REGAZZONI², AND D. RICCOBELLI²

ABSTRACT. Modeling the behavior of biological tissues and organs often necessitates the knowledge of their shape in the absence of external loads. However, when their geometry is acquired *in-vivo* through imaging techniques, bodies are typically subject to mechanical deformation due to the presence of external forces, and the load-free configuration needs to be reconstructed. This paper addresses this crucial and frequently overlooked topic, known as the inverse elasticity problem (IEP), by delving into both theoretical and numerical aspects, with a particular focus on cardiac mechanics. In this work, we extend Shield's seminal work to determine the structure of the IEP with arbitrary material inhomogeneities and in the presence of both body and active forces. These aspects are fundamental in computational cardiology, and we show that they may break the variational structure of the inverse problem. In addition, we show that the inverse problem might be ill-posed, even in the presence of constant Neumann boundary conditions and a polyconvex strain energy functional. We then present the results of extensive numerical tests to validate our theoretical framework, and to characterize the computational challenges associated with a direct numerical approximation of the IEP. Specifically, we show that this framework outperforms existing approaches both in terms of robustness and optimality, such as Sellier's iterative procedure, even when the latter is improved with acceleration techniques. A notable discovery is that multigrid preconditioners are, in contrast to standard elasticity, not efficient, and domain decomposition methods provide a much more reliable alternative. Finally, we successfully address the IEP for a full-heart geometry, demonstrating that the IEP formulation can compute the stress-free configuration in real-life scenarios where Sellier's algorithm proves inadequate.

1. INTRODUCTION

The objects we observe are rarely free from external mechanical stresses. For example, all bodies around us are subject to gravity. While such a force usually induces small displacements in stiffer materials, it can lead to large deformations in soft matter [42, 54, 41]. Furthermore, in biomedical applications, the shape of organs and tissues observed through medical imaging techniques are affected by the presence of mechanical forces that can significantly deform them. An important example in this respect is the heart: the presence of the ribcage and surrounding organs, as well as the blood pressure in the chambers, produce large deformations and it is not possible to observe its relaxed shape *in-vivo*. In fact, directly observing the configuration of an elastic body in the absence of external forces is far from being a trivial task.

In nonlinear elasticity, the task of reconstructing the relaxed configuration of a body subject to mechanical loads, hereafter referred to as the *inverse elasticity problem* (IEP), is a long-standing and largely overlooked problem, which is briefly cited in the Truesdell and Noll book as the *free shape problem* [61]. The problem has received little attention from the continuum mechanics community: it has been originally addressed by Shield [57] for homogeneous bodies in the absence of body forces, and has been extended by Merodio and Ogden [39] to take into account body forces. Up to our knowledge, Shield's theory has never been extended to the inhomogeneous case, despite it being fundamental in several application areas, including computational cardiology, since the fiber direction changes within the myocardium. Shield's theory has been exploited as a tool to identify analytical solutions in non-linear elasticity [15, 44, 30, 31, 14], but the structure of the IEP as a boundary value problem remains largely unexplored.

The IEP has received some more attention in the scientific computing community [38], where it is known as *inverse design problem* [28] or *prestress problem* [25]. Its role in the specific case of cardiac

(1) CENTRO DE MODELAMIENTO MATEMÁTICO, UNIVERSIDAD DE CHILE, AV. BEAUCHEF 851, SANTIAGO, CHILE

(2) MOX – DIPARTIMENTO DI MATEMATICA, POLITECNICO DI MILANO, PIAZZA LEONARDO DA VINCI 32, MILANO, 20133, ITALY

E-mail addresses: nbarnafi@cmm.uchile.cl, francesco.regazzoni@polimi.it, davide.riccobelli@polimi.it.

Corresponding author: F. Regazzoni.

modeling, and in biomechanics in general, is pivotal, as a reliable identification of the relaxed configuration is fundamental to correctly describe the stress distribution in soft tissues [37, 51]. A possible solution approach, based on a fixed-point algorithm, was proposed by Sellier [56] and allows for solving the inverse problem by leveraging only a solver for the direct problem. This approach is particularly attractive, as it allows to re-use existing software. However, when applied to real-life problems such as four-chamber cardiac geometries, it often presents convergence issues. To mitigate them, Sellier's method has been improved through adaptive continuation methods [51] and acceleration techniques [48, 37]. We highlight that the Sellier's method is not only relevant for cardiac simulations, and it has indeed also been used for modeling the eyes [40], aorta [25], and brain [43].

In this work, we study the IEP, with a special focus on the context of cardiac modeling. Our scope is twofold: on one hand, we study the mathematical structure of the IEP, extending Shield's theory to the case of inhomogeneous bodies subject to active forces. On the other hand, we thoroughly characterize this problem numerically for increasing levels of complexity and compare a direct numerical approximation of the latter with the Sellier method in terms of robustness with respect to external loads and its optimality.

The paper is organized as follows. In Section 2, we review some basic facts of non-linear elasticity and we derive the IEP, together with some remarks on the mathematical structure and some elementary examples. In Section 3, we derive the weak formulation for both the direct and the inverse elasticity problems. In Section 4, we show with simple examples the mechanisms through which the IEP problem can give rise to self-intersections. In Section 5 we describe all the algorithms that we consider for this study, which are (a) the Sellier method, (b) the Aitken accelerated Sellier method, (c) the Anderson accelerated Sellier method, and (d) the direct numerical approximation of the IEP. In Section 6 we provide several numerical tests with the scope of (a) validating our theoretical claims, (b) characterizing the computational burden of IEP, and (c) testing the methods in realistic cardiac contexts. We conclude our work in Section 7.

2. PROBLEM DESCRIPTION

In this section we describe both the direct elasticity problem (DEP) and the inverse elasticity problem (IEP). For the latter, we show how it can be re-cast in terms of the Eshelby tensor, which will provide a way to guarantee the existence of solutions of the IEP under some special conditions.

2.1. The direct problem of non-linear elasticity. We assume that a body occupies a given region Ω_0 of the three dimensional Euclidean space \mathbb{E}^3 . Let $\Omega \subset \mathbb{E}^3$ be the current configuration of the body, which is given by a deformation field χ such that $\Omega = \chi(\Omega_0)$. Specifically, the current position of the generic material point $\mathbf{X} \in \Omega_0$ is denoted by \mathbf{x} , i.e. $\mathbf{x} = \chi(\mathbf{X})$. The displacement field is thus defined as $\mathbf{u}(\mathbf{X}) := \chi(\mathbf{X}) - \mathbf{X}$. We denote by Grad and grad the gradient operators with respect to \mathbf{X} and \mathbf{x} , respectively. Similarly, we denote by Div and div the corresponding divergence operators.

We introduce the deformation gradient $\mathbf{F} := \text{Grad } \chi = \mathbf{I} + \text{Grad } \mathbf{u}$, together with the local volume change described by $J := \det \mathbf{F}$. Let \mathbf{P} be the Piola-Kirchhoff stress tensor, then under the assumption of quasi-static deformations, the balance of the linear momentum reads

$$(1) \quad \text{Div } \mathbf{P} + \mathbf{B} = \mathbf{0}, \quad \text{in } \Omega_0,$$

where \mathbf{B} is the density of body forces in the reference configuration. Such a balance equation can be also cast in current configuration by means of the Cauchy stress tensor

$$(2) \quad \mathbf{T} = J^{-1} \mathbf{P} \mathbf{F}^T.$$

More specifically, we get

$$(3) \quad \text{div } \mathbf{T} + \mathbf{b} = \mathbf{0},$$

where \mathbf{b} is the density of body force in the current configuration. The material and the spatial densities of force \mathbf{B} and \mathbf{b} are related by $\mathbf{B} = J\mathbf{b}$. For illustrative purposes, in this section, we assume that the boundary $\partial\Omega_0$ is composed of two distinct subsets, Γ_0^D and Γ_0^N , such that on Γ_0^D we prescribe the displacement field \mathbf{u}_D , and on we assume that

$$(4) \quad \mathbf{P} \mathbf{N} = \mathbf{t}_0 \quad \text{on } \Gamma_0^N,$$

where the traction load \mathbf{t}_0 is a (known) vector field over Γ_0^N . The Eulerian counterpart of (4) is

$$(5) \quad \mathbf{T} \mathbf{n} = \mathbf{t} \quad \text{on } \Gamma^N,$$

where $\mathbf{t} = J^{-1} \|\mathbf{F}^T \mathbf{n}\| \mathbf{t}_0$ and the normal vectors are related by $\mathbf{n} = \|\mathbf{F}^{-T} \mathbf{N}\|^{-1} \mathbf{F}^{-T} \mathbf{N}$.

In the context of hyperelasticity, we postulate the existence of a strain energy density $\Psi = \Psi(\mathbf{X}, \mathbf{F})$. Thus, by means of the Clausius-Duhem inequality, we obtain

$$\mathbf{P} = \mathbf{P}(\mathbf{X}, \mathbf{F}) = \frac{\partial \Psi}{\partial \mathbf{F}}, \quad P_{ij} = \frac{\partial \Psi}{\partial F_{ij}}.$$

In the next section, we discuss the inverse counterpart of the problem described in this section, the so called *inverse elasticity problem* (IEP).

2.2. The inverse elasticity problem. In solid mechanics, the DEP consists in reconstructing the current configuration given the reference configuration by solving (1), complemented by appropriate boundary conditions and by the constitutive assumptions on the material response. In what follows we are interested in the IEP instead: the reconstruction of the relaxed configuration Ω_0 given the current configuration Ω and the external loads. Consider the inverse deformation $\hat{\chi} = \chi^{-1}$, so that $\mathbf{X} = \hat{\chi}(\mathbf{x})$ and the inverse displacement is defined similarly to \mathbf{u} as $\hat{\mathbf{u}}(\mathbf{x}) = \hat{\chi}(\mathbf{x}) - \mathbf{x}$. The fields \mathbf{u} and $\hat{\mathbf{u}}$ are related through the deformation fields as

$$\mathbf{u} = -\hat{\mathbf{u}} \circ \chi, \quad \hat{\mathbf{u}} = -\mathbf{u} \circ \hat{\chi}.$$

Remark 1. In what follows, for the sake of conciseness, we will omit the composition with χ and $\hat{\chi}$, when this will be clear from the context, and we will simply write, for instance, $\mathbf{u} = -\hat{\mathbf{u}}$.

Remark 2. Unless specified differently, we restrict our attention to the situation in which the *reference configuration* coincides with the *relaxed configuration*, namely if \mathbf{F} is the identity \mathbf{I} , we have

$$\mathbf{P}(\mathbf{X}, \mathbf{I}) = \mathbf{0}.$$

We highlight that this might be restrictive, especially for living tissues, for which a relaxed configuration might not exist. Indeed, a variety of processes, such as growth [55, 18, 27], active phenomena [34, 59, 4, 53], and plastic deformations [35, 36], might produce local distortions that are geometrically incompatible. This leads to the generation of a stress state in the body even in the absence of external loads. The correct identification of the relaxed state of elastic bodies subject to these phenomena require specific treatments which go beyond the scope of the present article. Nonetheless, a remarkable case in which the theory described in this Section can be directly applied is the active stress approach, a method usually exploited to model contractility in muscle tissue. Such aspects are treated in Section 2.4.

We denote the inverse deformation gradient by $\hat{\mathbf{F}} = \text{grad } \hat{\chi} = \mathbf{I} + \text{grad } \hat{\mathbf{u}}$. The two deformation gradient tensors are related by $\hat{\mathbf{F}} = \mathbf{F}^{-1}$.

From (3), the IEP can be cast as finding $\hat{\mathbf{u}}$ such that

$$(6) \quad \begin{cases} \text{div } \mathbf{T}(\mathbf{x}, \hat{\mathbf{F}}^{-1}) + \mathbf{b} = \mathbf{0} & \text{in } \Omega, \\ \mathbf{T}(\mathbf{x}, \hat{\mathbf{F}}^{-1})\mathbf{n} = \mathbf{t} & \text{on } \Gamma^N, \\ \hat{\mathbf{u}} = -\mathbf{u}_D & \text{on } \Gamma^D. \end{cases}$$

It is well known that the direct problem has a variational structure, where the displacement field must minimize the functional

$$(7) \quad \mathcal{F}[\mathbf{u}] = \int_{\Omega_0} \Psi(\mathbf{X}, \mathbf{F}) \, d\mathbf{X} - \int_{\Gamma_0^N} \mathbf{t}_0 \cdot \mathbf{u} \, dS - \int_{\Omega_0} \mathbf{B} \cdot \mathbf{u} \, d\mathbf{X}.$$

We shall assume that Ψ is polyconvex, namely there exists a convex function $g : \text{Lin}^+(\mathbb{R}^3) \times \text{Lin}^+(\mathbb{R}^3) \times \mathbb{R}^+ \rightarrow \mathbb{R} \cup \{+\infty\}$ such that

$$\Psi(\mathbf{F}) = g(\mathbf{F}, \text{Cof } \mathbf{F}, J).$$

This condition, plus some growth conditions [9], guarantee that the DEP (1)-(4) admits a solution represented by a minimum of the functional (7). In what follows, we will show that the situation is more complex for the inverse problem (6).

2.2.1. Shield's transformation and convexity properties. Under the assumption of material homogeneity, the variational structure of the problem follows from *Shield's transformation* [57]. Such a transformation leads to an equivalent formulation of (3), where the Eshelby stress tensor Σ takes the place of the Cauchy stress \mathbf{T} . As noticed by Chadwick [16], such a correspondence suggests a duality between the Eshelby and the Cauchy stress tensors. In this section, we expand Shield's initial findings to encompass

inhomogeneous materials, employing a methodology akin to that elucidated in [39]. A simple change of variable shows that

$$\int_{\Omega_0} \Psi(\mathbf{X}, \mathbf{F}) \, dX = \int_{\Omega} J^{-1} \Psi(\boldsymbol{\chi}^{-1}(\mathbf{x}), \mathbf{F}) \, dx.$$

Thus, we introduce the dual energy density $\widehat{\Psi} = \widehat{\Psi}(\mathbf{x}, \widehat{\mathbf{F}})$, defined as

$$(8) \quad \widehat{\Psi}(\mathbf{x}, \widehat{\mathbf{F}}) = \widehat{J} \Psi(\widehat{\boldsymbol{\chi}}(\mathbf{x}), \widehat{\mathbf{F}}^{-1}).$$

Equation (8) is the Shield transformation of Ψ . We then introduce the spatial *Eshelby stress* Σ , defined as

$$(9) \quad \Sigma := \frac{\partial \widehat{\Psi}}{\partial \widehat{\mathbf{F}}} = \widehat{J} \widehat{\mathbf{F}}^{-T} (\Psi \mathbf{I} - \mathbf{P} \widehat{\mathbf{F}}^{-T}) = \widehat{\mathbf{F}}^{-T} (\widehat{\Psi} \mathbf{I} - \mathbf{T}).$$

Since

$$\frac{d}{dx_i} \widehat{\Psi}(\mathbf{x}, \widehat{\mathbf{F}}(\mathbf{x})) = \frac{\partial \widehat{\Psi}}{\partial x_i} + \sum_{h,k=1}^3 \frac{\partial \widehat{\Psi}}{\partial \widehat{F}_{hk}} \frac{\partial \widehat{F}_{hk}}{\partial x_i} = \frac{\partial \widehat{\Psi}}{\partial x_i} + \sum_{h,k=1}^3 \Sigma_{hk} \frac{\partial \widehat{F}_{hk}}{\partial x_i},$$

and

$$\begin{aligned} \frac{\partial}{\partial x_j} \left(\sum_{h=1}^3 \widehat{F}_{hi} \Sigma_{hj} \right) &= \sum_{h=1}^3 \left(\frac{\partial \widehat{F}_{hi}}{\partial x_j} \Sigma_{hj} + \widehat{F}_{hi} \frac{\partial \Sigma_{hj}}{\partial x_j} \right) = \\ &= \sum_{h=1}^3 \left(\frac{\partial \widehat{\Psi}}{\partial \widehat{F}_{hj}} \frac{\partial \widehat{F}_{hi}}{\partial x_j} + \widehat{F}_{hi} \frac{\partial \Sigma_{hj}}{\partial x_j} \right) = \\ &= \sum_{h=1}^3 \left(\frac{\partial \widehat{\Psi}}{\partial \widehat{F}_{hj}} \frac{\partial \widehat{F}_{hj}}{\partial x_i} + \widehat{F}_{hi} \frac{\partial \Sigma_{hj}}{\partial x_j} \right), \end{aligned}$$

from (9) we can rewrite the momentum equation in terms of the Eshelby stress tensor:

$$\begin{aligned} \text{div } \mathbf{T} &= \text{div}(\widehat{\Psi} \mathbf{I}) - \text{div}(\widehat{\mathbf{F}}^T \Sigma) = \\ &= \text{grad } \widehat{\Psi} - \text{div}(\widehat{\mathbf{F}}^T \Sigma) = \\ (10) \quad &= \frac{\partial \widehat{\Psi}}{\partial \mathbf{x}} + \Sigma : \text{grad } \widehat{\mathbf{F}} - \Sigma : \text{grad } \widehat{\mathbf{F}} - \widehat{\mathbf{F}}^T \text{div } \Sigma = \\ &= \frac{\partial \widehat{\Psi}}{\partial \mathbf{x}} - \widehat{\mathbf{F}}^T \text{div } \Sigma, \end{aligned}$$

where $\partial \widehat{\Psi} / \partial \mathbf{x}$ is the partial derivative of $\widehat{\Psi}(\mathbf{x}, \widehat{\mathbf{F}}(\mathbf{x}))$ with respect to its first argument. Thus, the problem (6) is equivalent to the following one expressed in terms of the Eshelby stress tensor

$$(11) \quad \begin{cases} \text{div } \Sigma + \boldsymbol{\beta} = \mathbf{0} & \text{in } \Omega, \\ \Sigma \mathbf{n} = \boldsymbol{\sigma} & \text{on } \Gamma^N, \\ \widehat{\mathbf{u}} = -\mathbf{u}_D & \text{on } \Gamma^D, \end{cases}$$

where, from (9) and (10), we have

$$(12) \quad \boldsymbol{\beta} = -\widehat{\mathbf{F}}^{-T} \left(\mathbf{b} + \frac{\partial \widehat{\Psi}}{\partial \mathbf{x}} \right), \quad \boldsymbol{\sigma} = \widehat{\mathbf{F}}^{-T} (\widehat{\Psi} \mathbf{n} - \mathbf{t}).$$

We remark that such a formulation holds for any constitutive assumptions and, up to our knowledge, it has not been reported elsewhere. Previous derivations all assume that the body is homogeneous, i.e. $\widehat{\Psi}$ does not depend on \mathbf{x} . This is relevant for anisotropic materials, and more so in cardiac mechanics since the direction of the fibers usually depends on \mathbf{x} , rendering the term $\boldsymbol{\beta}$ in (11) not zero even in the absence of body forces. We have summarized the main quantities involved in the direct and the inverse formulations in Table 1.

In the particular case of homogeneous materials ($\partial \widehat{\Psi} / \partial \mathbf{x} = 0$), problem (11) can be written as a minimization problem assuming that $\boldsymbol{\beta}$ and $\boldsymbol{\sigma}$ are measurable functions depending only on space:

$$(13) \quad \boldsymbol{\beta} : \Omega \rightarrow \mathbb{R}^3, \quad \boldsymbol{\sigma} : \Omega \rightarrow \mathbb{R}^3.$$

Quantity	Direct	Inverse (Cauchy)	Inverse (Eshelby)
Energy	$\Psi(\mathbf{F})$	–	$\widehat{\Psi}(\widehat{\mathbf{F}}) = \widehat{J}\Psi(\widehat{\mathbf{F}}^{-1})$
Stress	$\mathbf{P}(\mathbf{F})$	$\mathbf{T}(\widehat{\mathbf{F}}^{-1}) = \widehat{J}\mathbf{P}(\widehat{\mathbf{F}}^{-1})\widehat{\mathbf{F}}^{-T}$	$\boldsymbol{\Sigma}(\widehat{\mathbf{F}}) = \widehat{\mathbf{F}}^{-T} \left(\widehat{\Psi}(\widehat{\mathbf{F}})\mathbf{I} - \mathbf{T}(\widehat{\mathbf{F}}^{-1}) \right)$
Volume load	\mathbf{B}	$\mathbf{b} = \widehat{J}\mathbf{B}$	$\boldsymbol{\beta} = -\widehat{\mathbf{F}}^{-T} \left(\mathbf{b} + \partial\widehat{\Psi}/\partial\mathbf{x} \right)$
Surface load	\mathbf{t}_0	$\mathbf{t} = \widehat{J}\ \mathbf{F}^T\mathbf{n}\ \mathbf{t}_0$	$\boldsymbol{\sigma} = \widehat{\mathbf{F}}^{-T}(\widehat{\Psi}\mathbf{n} - \mathbf{t})$

TABLE 1. Energy, stress, and load terms in all three formulations: DEP (1), IEP in terms of the Cauchy stress (6) and of the Eshelby stress (11). We omit the explicit dependence on \mathbf{X} and \mathbf{x} .

Then, under these assumptions, it can be seen that (11) is equivalent to finding the stationary points of the functional

$$(14) \quad \widehat{\mathcal{F}}[\widehat{\mathbf{u}}] = \int_{\Omega} \widehat{\Psi}(\widehat{\mathbf{F}}) \, dx - \int_{\Gamma^N} \boldsymbol{\sigma}(\mathbf{x}) \cdot \widehat{\mathbf{u}}(\mathbf{x}) \, dS - \int_{\Omega} \boldsymbol{\beta}(\mathbf{x}) \cdot \widehat{\mathbf{u}}(\mathbf{x}) \, dx.$$

Remarkably, Shield’s transformation (8) preserves polyconvexity or rank-1 convexity if Ψ is polyconvex or rank-1 convex as well, see Proposition 17.6.2 in [58]. Ball’s theorem on the existence of energy minimizers [9] can then be used to prove the existence of minimizers (14).

However, in practical applications, this is almost never the case. Indeed, the existence theorem can be applied if $\boldsymbol{\beta}$ and $\boldsymbol{\sigma}$ are functions of \mathbf{x} only, as assumed in (13), but, in most applications, $\boldsymbol{\beta}$ and $\boldsymbol{\sigma}$ depend on $\widehat{\mathbf{F}}$ as well, and (11) is not anymore equivalent to finding the stationary points of (14). This aspect can create some issues as shown in the following two examples.

2.2.2. Elastic disk subject to an external pressure: non-existence of radially symmetric solutions. Consider now the circular domain $\Omega = B(O, r_o) \subset \mathbb{E}^2$ representing the current configuration, where $B(O, r_o)$ is the disk of center O and radius r_o . Let (R, Θ) and (r, θ) be the reference and the spatial polar coordinates of a generic point about the origin O . We assume that the sphere is subject to a pressure p_{ext} , so that

$$(15) \quad \mathbf{T}\mathbf{e}_r = -p_{\text{ext}}\mathbf{e}_r,$$

where $(\mathbf{e}_R, \mathbf{e}_{\Theta})$ and $(\mathbf{e}_r, \mathbf{e}_{\theta})$ are the polar basis in the reference and in the current configuration, respectively. We assume that the material behaves as a compressible Neo-Hookean material, given by a strain energy density defined as

$$(16) \quad \Psi(\mathbf{F}) = \frac{\mu}{2}(\text{tr}(\mathbf{F}^T\mathbf{F}) - 2) + \frac{\lambda}{2}(\log J)^2,$$

where λ and μ are the (linear) Lamé’s parameters. Under such assumptions, the Cauchy stress tensor reads

$$(17) \quad \mathbf{T} = \frac{1}{J} \left(\mu\mathbf{F}\mathbf{F}^T + (\lambda \log J - \mu)\mathbf{I} \right).$$

We assume polar symmetry, so that $r = r(R)$ and $\theta = \Theta$. The deformation gradient is given by

$$\mathbf{F} = r'\mathbf{e}_r \otimes \mathbf{e}_R + \frac{r}{R}\mathbf{e}_{\theta} \otimes \mathbf{e}_{\Theta}.$$

Due to the symmetries of the deformation field, the balance of linear momentum (3) reduces to the following ordinary differential equation

$$(18) \quad \frac{dT_{rr}}{dr} + \frac{T_{rr} - T_{\theta\theta}}{r} = 0.$$

We observe that $r = r_o R/R_o$ satisfies (18). Here, $R_o \in \mathbb{R}$ is the reference radius of the disk that can be found by enforcing the boundary condition (15), obtaining

$$(19) \quad \frac{R_o^2}{r_o^2} \lambda \log \left(\frac{r_o^2}{R_o^2} \right) + \left(1 - \frac{R_o^2}{r_o^2} \right) \mu = -p_{\text{ext}},$$

whose solution can be expressed as

$$R_o^2 = (\mu + p_{\text{ext}}) \left(\lambda W_0 \left(\frac{e^{\mu/\lambda}(\mu + p_{\text{ext}})}{\lambda} \right) \right)^{-1} r_o^2,$$

where W_0 is the principal branch of the Lambert function ($w = W_0(z)$ is the solution of $we^w = z$, with z being a complex number), see Fig. 1. In the special case $\lambda = 0$, the solution of (19) is given by

$$R_o^2 = \frac{\mu + p_{\text{ext}}}{\mu}.$$

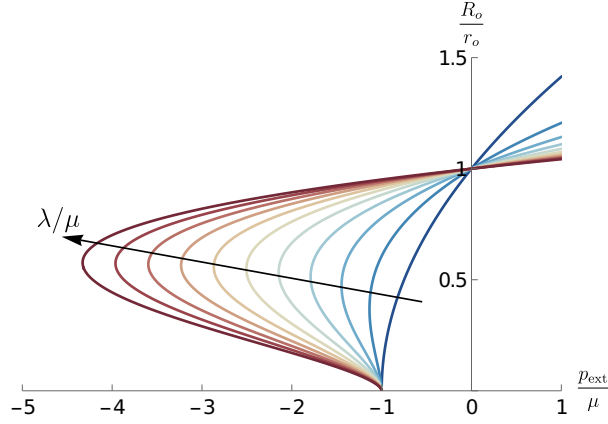


FIGURE 1. Plot of R_o/r_o as a function of p_{ext}/μ for $\lambda/\mu = 0, 1, \dots, 10$. The arrow denotes the direction in which λ/μ increases.

We observe that depending on the value of the applied pressure, the inverse problem may not have solutions with radial symmetry. In particular, $R_o = 0$ is a solution for the inverse problem for

$$p_{\text{ext}} = -\mu.$$

and for all the values of λ . This is a limit case where the reference configuration shrinks to a single point for a finite value of the external pressure. Thus, the IEP might be ill-posed even if we apply constant Neumann boundary conditions and if we choose a polyconvex strain energy density.

2.3. Injectivity of the inverse deformation. Usually, the deformation field is supposed to be bijective to avoid self-intersections of the body. However, requiring that $\hat{\chi}$ be bijective might be too strict for the free body problem. Indeed, if we take two S-shaped pieces, we can imagine to glue them together, as shown in Fig. 2, and the relaxed state of the body requires a self-intersection. This situation is not uncommon and, as shown in the following paragraphs, applies to the heart as well.

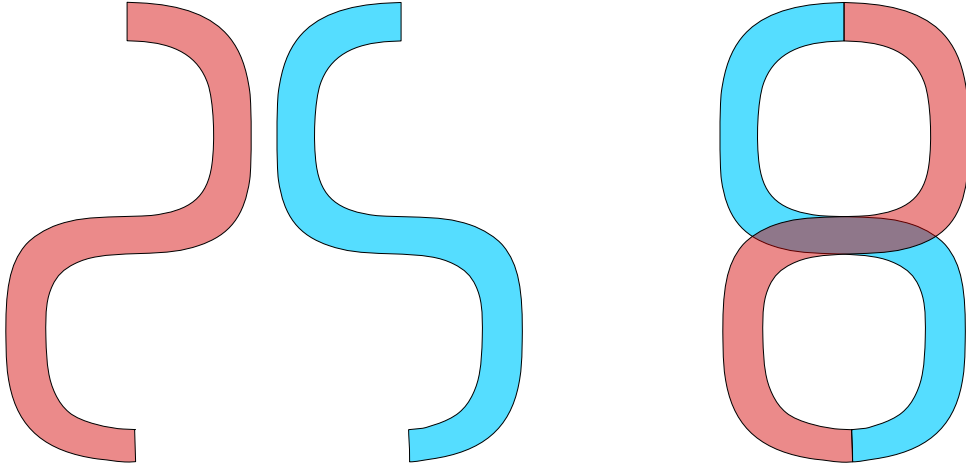


FIGURE 2. Left: representation of two symmetric S-shaped pieces in their relaxed configuration. Right: relaxed state of the two pieces after they are glued together; the relaxed state of the body exhibits a self-intersection.

Thus, the relaxed configuration of the body can not in general be achievable in reality due to a global geometric incompatibility, i.e. $\hat{\chi}$ is not injective. The analysis proposed in this section is still valid since χ is locally invertible due to the inverse function theorem ($J = \det \text{Grad } \chi > 0$).

Some issues may arise if we want to describe a further deformation of Ω to $\bar{\Omega}$ with $\bar{\Omega} = \bar{\chi}(\Omega)$. In such a case, the relaxed configuration Ω_0 cannot be used as a reference configuration due to the self-intersection of the body. A possible strategy to solve such a problem is to take Ω as a reference configuration. In such a case, similarly to the multiplicative decomposition of the deformation gradient exploited to model plasticity [35, 36], growth and remodelling [55, 20], we introduce

$$\mathbf{F}_e = \bar{\mathbf{F}}\hat{\mathbf{F}}^{-1},$$

where $\bar{\mathbf{F}} = \text{grad } \bar{\chi}$ and \mathbf{F}_e is the elastic distortion from the relaxed state to the configuration $\bar{\Omega}$. Then, the strain energy density per unit volume of Ω is given by

$$\psi(\bar{\mathbf{F}}) = (\det \hat{\mathbf{F}})\Psi(\mathbf{F}_e).$$

This underlines the possibility to treat local and global geometric incompatibilities in a unique way. The local incompatibilities manifest themselves as a non-compatible $\hat{\mathbf{F}}$, i.e. there does not exist a function $\hat{\chi}$ such that $\hat{\mathbf{F}} = \text{grad } \hat{\chi}$ [52], while a global geometric incompatibility is a non-injectivity of $\hat{\chi}$. The inclusion of local geometric incompatibilities of the relaxed state in the IEP is left as a possible future study.

2.4. Active stress. When modeling biological tissues, and the myocardium in particular, it is important to take into account the active forces that are involved during muscle contraction. One of these approaches is the so called *active stress*. Usually it is assumed that there exists a reference configuration Ω_0 that is *stress free in the absence of active forces* [4, 53]. Let $\Psi_{\text{pas}}(\mathbf{X}, \mathbf{F})$, be the strain energy density of the passive material, and we introduce the passive first Piola-Kirchhoff stress tensors, defined as

$$(20) \quad \mathbf{P}_{\text{pas}}(\mathbf{X}, \mathbf{F}) := \frac{\partial \Psi_{\text{pas}}}{\partial \mathbf{F}}.$$

We require \mathbf{P}_{pas} to satisfy

$$\mathbf{P}_{\text{pas}}(\mathbf{X}, \mathbf{I}) = 0 \quad \forall \mathbf{X} \in \Omega_0.$$

Let $\mathbf{P}_{\text{act}}(\mathbf{X}, \mathbf{F}; T_a)$ be a tensor-valued function representing the active stress generated by the muscle fiber contractility. Here, T_a is a parameter describing the tension generated by the muscle, which is zero in the passive case. Hence, we assume that $\mathbf{P}_{\text{act}}(\mathbf{X}, \mathbf{F}; 0) = 0$. The active stress approach envisages writing first Piola-Kirchhoff stress tensor as

$$(21) \quad \mathbf{P} = \mathbf{P}_{\text{pas}} + \mathbf{P}_{\text{act}}.$$

In conclusion, when considering active materials, the IEP shall be regarded as that of finding the configuration assumed by the body in the absence of both passive and active stress, that is when $\mathbf{P}_{\text{pas}} = \mathbf{P}_{\text{act}} = 0$.

2.4.1. Active stress in cardiac mechanics problems. As it is standard in the cardiac modeling literature, we consider an orthonormal triplet $(\mathbf{e}_f, \mathbf{e}_s, \mathbf{e}_n)$ of fibers, sheets, sheet-normal directions [46, 12]. The fiber architecture plays a role in determining both the passive and the active response of the tissue. A common choice for the active stress tensor is

$$(22) \quad \mathbf{P}_{\text{act}} = S_f(\|\mathbf{F}\mathbf{e}_f\|; T_a) \frac{\mathbf{F}\mathbf{e}_f \otimes \mathbf{e}_f}{\|\mathbf{F}\mathbf{e}_f\|} + S_n(\|\mathbf{F}\mathbf{e}_n\|; T_a) \frac{\mathbf{F}\mathbf{e}_n \otimes \mathbf{e}_n}{\|\mathbf{F}\mathbf{e}_n\|},$$

where S_f and S_n are scalar functions. We remark that, if S_f and S_n are integrable with respect to $\|\mathbf{F}\mathbf{e}_f\|$ and $\|\mathbf{F}\mathbf{e}_n\|$, respectively, and ψ_f and ψ_n are their primitives, we have [26, 50].¹

$$(23) \quad \mathbf{P}_{\text{act}} = \frac{\partial \psi_f}{\partial \mathbf{F}} + \frac{\partial \psi_s}{\partial \mathbf{F}} = \frac{\psi'_f(\|\mathbf{F}\mathbf{e}_f\|; T_a)}{\|\mathbf{F}\mathbf{e}_f\|} \mathbf{F}\mathbf{e}_f \otimes \mathbf{e}_f + \frac{\psi'_n(\|\mathbf{F}\mathbf{e}_n\|; T_a)}{\|\mathbf{F}\mathbf{e}_n\|} \mathbf{F}\mathbf{e}_n \otimes \mathbf{e}_n,$$

where $'$ denotes the differentiation with respect to the first argument. Thus, the total (passive and active) stress tensor can be associated with the strain energy density:

$$(24) \quad \Psi(\mathbf{X}, \mathbf{F}; T_a) = \Psi_{\text{pas}}(\mathbf{F}) + \Psi_f(\|\mathbf{F}\mathbf{e}_f\|; T_a) + \Psi_n(\|\mathbf{F}\mathbf{e}_n\|; T_a).$$

In light of this observation, the procedure exposed in Section 2.2.1 can be applied to the energy ψ defined in (24).

¹As shown for skeletal muscles where a single family of fiber is present [26], such an approach is equivalent to model the tissue as a mixture of passive and active elements, for details see [53].

3. NUMERICAL APPROXIMATION

In this section, we provide the details to solve numerically equation (6). For this, we provide (i) the weak formulation, (ii) a detailed description of the IEP formulation for cardiac modeling, and (iii) a simple implementation of the IEP to show that an existing DEP solver can be turned into an IEP solver with little modifications.

3.1. Weak formulation. The weak formulation of the DEP (1) can then be stated as finding $\mathbf{u} \in V_0^{\mathbf{u}_D}$ such that

$$(25) \quad \int_{\Omega_0} \mathbf{P}(\mathbf{X}, \mathbf{F}) : \text{Grad } \mathbf{v} \, dX + \int_{\Gamma_0^N} \mathbf{t}_0 \cdot \mathbf{v} \, dS = \int_{\Omega_0} \mathbf{B} \cdot \mathbf{v} \, dX, \quad \forall \mathbf{v} \in V_0,$$

where we have defined the trial and test function spaces:

$$\begin{aligned} V_0^{\mathbf{u}_D} &= \{\mathbf{v} \in H^1(\Omega_0; \mathbb{R}^3) \text{ s.t. } \mathbf{v} = \mathbf{u}_D \text{ on } \Gamma_0^D\}, \\ V_0 &= \{\mathbf{v} \in H^1(\Omega_0; \mathbb{R}^3) \text{ s.t. } \mathbf{v} = \mathbf{0} \text{ on } \Gamma_0^D\}, \end{aligned}$$

and the weak formulation of the IEP can be stated as finding $\hat{\mathbf{u}} \in V^{\mathbf{u}_D}$ such that

$$(26) \quad \int_{\Omega} \mathbf{T}(\mathbf{x}, \hat{\mathbf{F}}^{-1}) : \text{grad } \mathbf{v} \, dx + \int_{\Gamma^N} \mathbf{t} \cdot \mathbf{v} \, ds = \int_{\Omega} \mathbf{b} \cdot \mathbf{v} \, dx, \quad \forall \mathbf{v} \in V,$$

where

$$\begin{aligned} V^{\mathbf{u}_D} &= \{\mathbf{v} \in H^1(\Omega; \mathbb{R}^3) \text{ s.t. } \mathbf{v} = -\mathbf{u}_D \text{ on } \Gamma^D\}, \\ V &= \{\mathbf{v} \in H^1(\Omega; \mathbb{R}^3) \text{ s.t. } \mathbf{v} = \mathbf{0} \text{ on } \Gamma^D\}, \end{aligned}$$

and we recall that

$$\mathbf{T}(\mathbf{x}, \hat{\mathbf{F}}^{-1}) = \hat{\mathbf{J}} \mathbf{P}(\hat{\chi}(\mathbf{x}), \hat{\mathbf{F}}^{-1}) \hat{\mathbf{F}}^{-T}.$$

Similarly, an equivalent weak formulation of (26) using the strong formulation (11) reads

$$(27) \quad \int_{\Omega} \Sigma(\mathbf{x}, \hat{\mathbf{F}}) : \text{grad } \mathbf{v} \, dx + \int_{\Gamma^N} \boldsymbol{\sigma} \cdot \mathbf{v} \, ds = \int_{\Omega} \boldsymbol{\beta} \cdot \mathbf{v} \, dx, \quad \forall \mathbf{v} \in V,$$

where the Eshelby stress tensor Σ is defined in (9).

3.2. Cardiac inverse model. In this section, we derive the IEP in the setting of cardiac modeling. Specifically, we account for the presence of an active stress and of cardiac fibers, and we consider boundary conditions often used to account for the interactions of the heart with the blood and with the surrounding organs.

3.2.1. The direct problem.

Geometry. Let Ω_0 be the stress-free configuration of the passive myocardium, and Ω the deformed configuration. We include in the domain also segments of the main vessels connecting the heart to the circulatory system (aorta, pulmonary artery and main veins). Typically, geometries available from medical imaging are acquired at diastasis, namely one of the last phases of diastole, right before the atrial kick (the beginning of atrial systole). This phase of the heartbeat is the one in which the heart is most stationary, thus facilitating the medical imaging acquisition process. Furthermore, being inertial forces negligible, a quasi-static assumption is well motivated at this stage. At diastasis, the blood pressures in the four chambers are relatively small, compared to the rest of the heartbeat, and active forces are also small. These features facilitate the IEP resolution.

Constitutive assumptions. We use the active stress approach described in Section 2.4 to model myocardium contractility. Specifically, we adopt the active stress tensor as in (22)-(23), where we choose [51]

$$(28) \quad \psi_f(\|\mathbf{F}\mathbf{e}_f\|) = T_a \|\mathbf{F}\mathbf{e}_f\|, \quad \psi_s(\|\mathbf{F}\mathbf{e}_s\|) = \alpha_n T_a \|\mathbf{F}\mathbf{e}_s\|,$$

where T_a denotes the active tension, acting mainly in the direction of fibers \mathbf{e}_f . The fibers are not perfectly aligned due to fiber dispersion. This is modeled through the introduction of the constant parameter $0 < \alpha_n < 1$ in (28). The Piola-Kirchhoff stress tensor thus reads [26, 51]

$$\mathbf{P} = \frac{\partial \Psi_{\text{pas}}(\mathbf{X}, \mathbf{F})}{\partial \mathbf{F}} + T_a \left[\frac{\mathbf{F}\mathbf{e}_f \otimes \mathbf{e}_f}{\|\mathbf{F}\mathbf{e}_f\|} + \alpha_n \frac{\mathbf{F}\mathbf{e}_n \otimes \mathbf{e}_n}{\|\mathbf{F}\mathbf{e}_n\|} \right],$$

We remark that, while solving the IEP for cardiac models, the active stress term is often neglected. However, it is important to notice that in any moment of the heartbeat (even at diastasis), a non-negligible amount of active tension is present, known as diastolic tension [32, 49]. Hence, it is crucial to account for the active stress during the stress-free configuration recovery procedure.

As a constitutive choice for the passive contribution to the strain energy density (see (20)-(21)), we use a function $\Psi_{\text{pas}}(\mathbf{X}, \mathbf{F})$, where the explicit dependence on \mathbf{X} is necessary to account for the anisotropic behaviour induced by the presence of muscle fibers. We use different expressions for Ψ_{pas} , which are explicitly specified in what follows.

Boundary conditions. We split the boundary $\partial\Omega_0$ of the domain in different subsets, and apply boundary conditions depending on the interacting tissues within each subset. The internal boundaries of the myocardium are in contact with blood, which exerts a pressure on the myocardium. We consider $N_{\text{cav}} = 6$ cavities (namely the four cardiac chambers, the aorta and the pulmonary artery), in which the blood pressure can be reasonably considered constant. For each cavity i (with $i = 1, \dots, N_{\text{cav}}$), we denote its boundary in the reference configuration by $\Gamma_0^{\text{endo},i} \subset \partial\Omega_0$. We model the action of the blood on the cavity surfaces as a constant hydrostatic pressure p_i :

$$\mathbf{P}\mathbf{N} = -p_i \mathbf{J}\mathbf{F}^{-T}\mathbf{N} \quad \text{on } \Gamma_0^{\text{endo},i}.$$

The epicardium, that is the external surface of the heart, is instead in contact with the pericardium, a tough fibroelastic sac containing the heart and the roots of the great vessels. We model the interaction of the heart with the pericardium by applying (anisotropic) linear springs on the pericardial surface Γ_0^{epi} [51, 45]:

$$(29) \quad \mathbf{P}\mathbf{N} = -K_n(\mathbf{N} \otimes \mathbf{N})\mathbf{u} - K_t(\mathbf{I} - \mathbf{N} \otimes \mathbf{N})\mathbf{u} \quad \text{on } \Gamma_0^{\text{epi}},$$

where the positive coefficients K_n and K_t account for the elastic response of the pericardium and the surrounding organs in the normal and tangent direction, respectively.

Finally, we apply homogeneous Dirichlet boundary conditions on the artificial boundaries originating where arteries and veins are truncated, which we denote by Γ_0^{D} .

Weak formulation. In conclusion, the weak formulation of the DEP consists in finding $\mathbf{u} \in V_0 = \{\mathbf{v} \in H^1(\Omega_0; \mathbb{R}^3) \text{ s.t. } \mathbf{v} = \mathbf{0} \text{ on } \Gamma_0^{\text{D}}\}$ such that

$$(30) \quad \begin{aligned} \int_{\Omega_0} \mathbf{P}(\mathbf{F}) : \text{Grad } \mathbf{v} \, dx = & - \sum_{i=1}^{N_{\text{cav}}} \int_{\Gamma_0^{\text{endo},i}} p_i \mathbf{J}\mathbf{F}^{-T}\mathbf{N} \cdot \mathbf{v} \, ds \\ & - \int_{\Gamma_0^{\text{epi}}} K_t \mathbf{u} \cdot \mathbf{v} \, ds \\ & - \int_{\Gamma_0^{\text{epi}}} (K_n - K_t) (\mathbf{N} \cdot \mathbf{u}) (\mathbf{N} \cdot \mathbf{v}) \, ds \end{aligned}$$

for all $\mathbf{v} \in V_0$.

3.2.2. The inverse problem. By proceeding as above, we derive the following IEP formulation for the cardiac model: we look for $\hat{\mathbf{u}} \in V = \{\mathbf{v} \in H^1(\Omega; \mathbb{R}^3) \text{ s.t. } \mathbf{v} = \mathbf{0} \text{ on } \Gamma^{\text{D}}\}$ such that

$$(31) \quad \begin{aligned} \int_{\Omega} \hat{\mathbf{J}}\mathbf{P}(\hat{\mathbf{F}}^{-1})\hat{\mathbf{F}}^{-T} : \text{grad } \mathbf{v} \, dx = & - \sum_{i=1}^{N_{\text{cav}}} \int_{\Gamma^{\text{endo},i}} p_i \mathbf{n} \cdot \mathbf{v} \, ds \\ & + \int_{\Gamma^{\text{epi}}} K_t \hat{\mathbf{J}} \|\hat{\mathbf{F}}^{-T} \mathbf{n}\| \hat{\mathbf{u}} \cdot \mathbf{v} \, ds \\ & + \int_{\Gamma^{\text{epi}}} (K_n - K_t) \frac{\hat{\mathbf{J}}}{\|\hat{\mathbf{F}}^{-T} \mathbf{n}\|} (\hat{\mathbf{F}}^{-T} \mathbf{n} \cdot \hat{\mathbf{u}}) (\hat{\mathbf{F}}^{-T} \mathbf{n} \cdot \mathbf{v}) \, ds \end{aligned}$$

for all $\mathbf{v} \in V$.

3.3. Remarks on implementation. In this section, we show that it is very simple to modify a solver for problem (25) to obtain a solver for problem (26), at least when relying on an automatic differentiation engine. To show this, we will provide an example using the Unified Form Language (UFL) [3], but the concepts are still valid for other equivalent systems. We start by looking at how a simple formulation of nonlinear elasticity could look like in Listing 1, which can be found among the demos at the documentation of FEniCS [2].

To convert this formulation, we need to (i) push forward the objects in the integrals and (ii) recast the kinematic quantities in terms of the inverse displacement. For this we have to observe that the Piola-Kirchhoff tensor is *still* the derivative of Ψ with respect to \mathbf{F} . This yields the formulation shown in Listing 2, where it can be seen that the difference between both codes is limited.

```

V = VectorFunctionSpace(mesh, 'CG', 1)
u = Function(V)
v = TestFunction(V)
F = variable(grad(u) + Identity(3)) # Compute original one to diff
J = det(F)
Cbar = J**(-2/3) * F.T * F
E, nu = 1.0e4, 0.3
mu = Constant(E/(2*(1 + nu)))
lmbda = Constant(E*nu/((1 + nu)*(1 - 2*nu)))
psi = (mu / 2) * (tr(Cbar) - 3) + 0.5 * lmbda * (J-1) * ln(J)
P = diff(psi, F)
residual = inner(P, grad(v)) * dx - dot(Constant((0,0,-1)), v)* dx
bcs = DirichletBC(V, Constant((0,0,0)), "on_boundary")
solve(residual==0, u, bcs=bcs)

```

LISTING 1. UFL formulation of (25).

```

V = VectorFunctionSpace(mesh, 'CG', 1)
u_hat = Function(V)
v = TestFunction(V)
F_hat = Identity(3) + grad(u_hat) # Inverse tensor for inverse problem
J_hat = det(F_hat)
F = variable(inv(F_hat)) # Compute original one to differentiate
J = det(F)
Cbar = J**(-2/3) * F.T * F
E, nu = 1.0e4, 0.3
mu = Constant(E/(2*(1 + nu)))
lmbda = Constant(E*nu/((1 + nu)*(1 - 2*nu)))
psi = (mu / 2) * (tr(Cbar) - 3) + 0.5 * lmbda * (J-1) * ln(J)
P = diff(psi, F)
residual = (J_hat * inner(P, grad(v) * inv(F_hat)) * dx
            - J_hat * dot(Constant((0,0,-1)), v)* dx)
bcs = DirichletBC(V, Constant((0,0,0)), "on_boundary")
solve(residual==0, u_hat, bcs=bcs)

```

LISTING 2. UFL formulation of (26).

4. SELF-INTERSECTION OF THE STRESS-FREE STATE

In this section, we discuss several aspects regarding the existence of a stress-free configuration. For this, we consider two simple geometries that represent a transverse cut of an idealized left ventricle as displayed in Figure 3. We refer to them as (a) the semi-circle and (b) the eclipse.

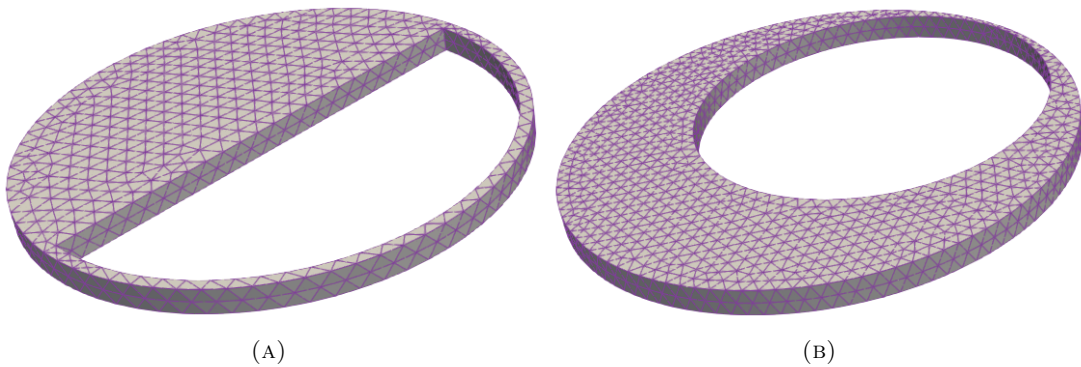


FIGURE 3. (a) Semi-circle and (b) eclipse meshes used to study self-intersection mechanisms in the inverse displacement problem.

As discussed in Section 2.3, a global geometric incompatibility can result into self-intersecting relaxed states. We show two mechanisms under which this phenomenon can be seen, namely inner self-intersections and outer self-intersections. We show this in the presented geometries by considering the inner surface as an endocardium where a given pressure is known, and on the epicardium we consider the elastic response that arises from the interaction with the pericardium.

We first load the semi-circle geometry with an endocardial pressure of 400 Pa, and we solve under these conditions the inverse displacement problem (26). The solution is displayed in Figure 4, where the thicker part of the geometry virtually does not deform, and indeed all deformation is obtained from the thinner part of the geometry. This results in an endocardial interpenetration. We proceed analogously with the eclipse, where we depict the solution in Figure 5. In contrast to the semi-circle case, here we see that there is a self-intersection through the epicardium.

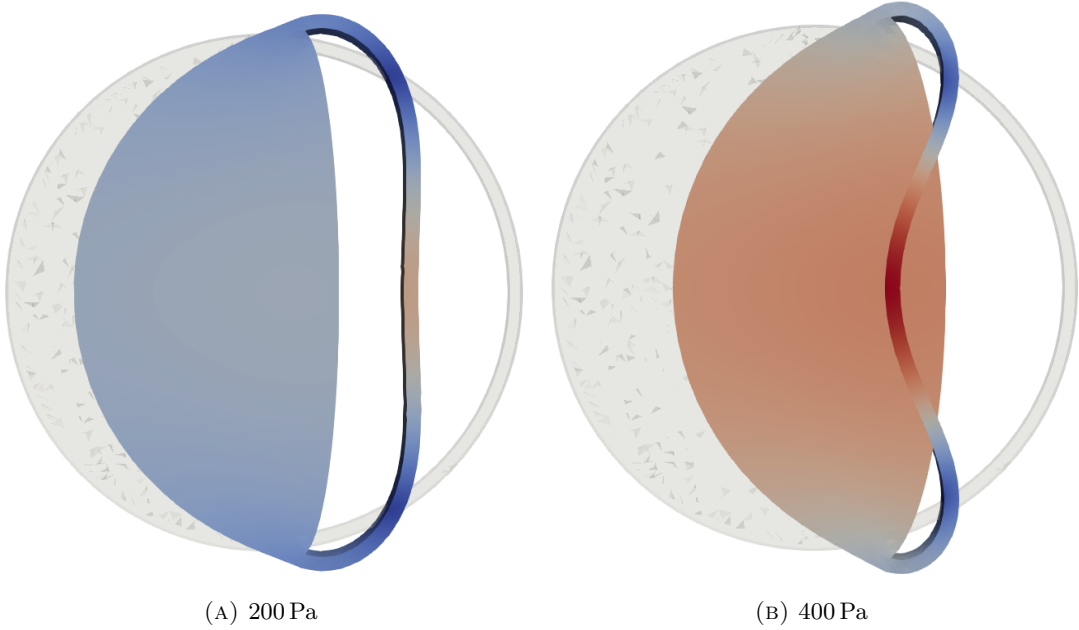


FIGURE 4. Solution of the inverse displacement problem on the semi-circle geometry. The stress-free configuration is computed for (a) 200 Pa and (b) 400 Pa.

These two examples of self-intersection represent a global geometric incompatibilities as detailed in Section 2.3, but they are still the solution obtained through the inverse displacement problem (26). This means that, unless a contact formulation is used, there is no guarantee that the stress-free configuration will avoid self-penetrations. Furthermore, it is not trivial to formulate a contact inverse displacement problem that is compatible with the forward problem.

5. ALGORITHMS FOR SOLVING THE INVERSE PROBLEM

There are essentially two approaches for solving (26). The first one is to solve the weak formulation associated with the inverse problem (26), e.g. by the Newton-Raphson method, and the second one is to leverage only (25), known as the Sellier method. The target problem is computationally challenging in both formulations, so we use a simple homotopy strategy to increase the loading terms with a fixed step size, i.e. by ramping the loads. We will denote this operation with a pseudo-time parameter, such that a load \mathbf{f} becomes $\mathbf{f}(t) = t\mathbf{f}$, with t in $[0, 1]$ being the ramp parameter. The desired solution is obtained when $t = 1$. We show how to solve the inverse displacement problem with this strategy in Algorithm 1, where the solution of problem (26) is done with a Newton algorithm. Unless stated otherwise, all nonlinear algorithms consider as initial guess the solution at the previous step.

The most widely used method to compute the solution of (26) is known as the Sellier method [56]. If we consider a relaxation parameter $\alpha > 0$ and an initial displacement $\mathbf{u}^{(0)}$, Denoting by $\Omega(\mathbf{X}^k)$ the configuration obtained in the \mathbf{X}^k coordinates, the algorithm is displayed in Algorithm 2. This method is a fixed-point iteration, which are in general prone to instabilities and lack of convergence. This has been alleviated by including an acceleration technique known as Aitken acceleration [48], and

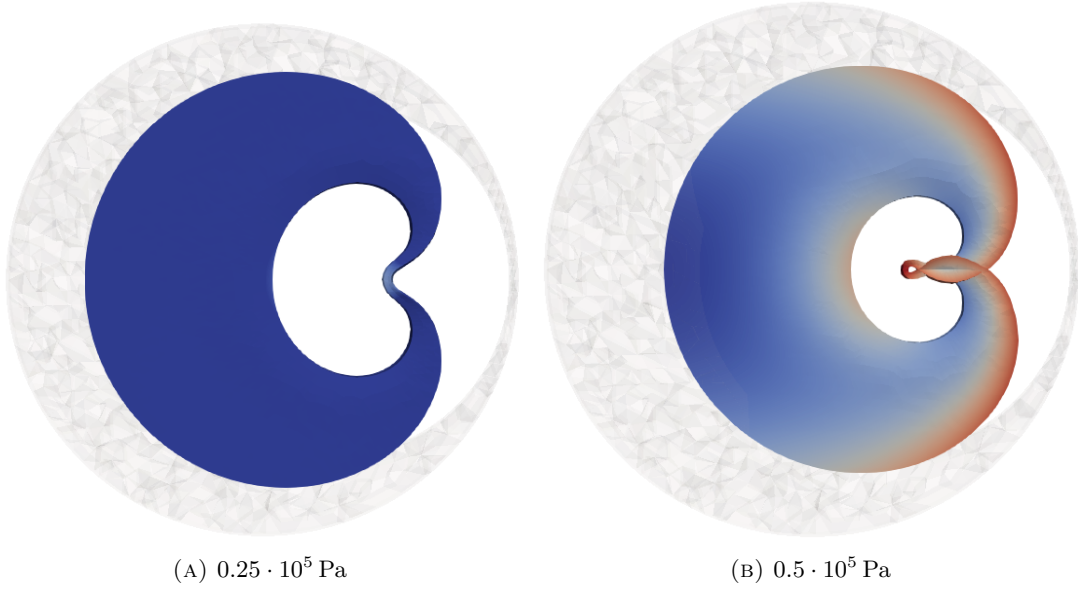


FIGURE 5. Solution of the inverse displacement problem on the eclipse geometry. The stress-free configuration is computed for (a) $0.25 \cdot 10^5$ Pa and (b) $0.5 \cdot 10^5$ Pa.

Algorithm 1 Inverse displacement method with load ramp.

- 1: **Input:** Initial point \mathbf{u}^0 , N
 - 2: Set **error** = 1, $k = 0$, $\Delta t = 1/N$, $t = \Delta t$, $\mathbf{u}^k = \mathbf{u}^0$
 - 3: **while** $t \leq 1$ **do**
 - 4: Compute solution \mathbf{d}^k of (26) at pseudo-instant t .
 - 5: $t \leftarrow t + \Delta t$
 - 6: **end while**
 - 7: **return** Solution $\mathbf{d} = \mathbf{d}^k$
-

further improved by an Armijo line search strategy [37]. We will refer to the latter as the Aitken-Armijo strategy. The resulting method enjoys improved robustness, which makes it more reliable for data intensive applications. Still, it has been observed that Anderson acceleration performs better than Aitken acceleration in most practical applications (see for example [13, 17]). This can be explained mainly by two things: on one hand, Anderson acceleration can be regarded as a nonlinear variant of the GMRES algorithm, so it has better mathematical foundations. On the other hand, it uses an arbitrary number of previous iterations, whereas Aitken uses only one previous solution. We propose a single algorithm that can be used to choose between the Armijo-Aitken strategy and Anderson acceleration in Algorithm 3, where we have observed that combining both Aitken and Anderson never yields a better solver (not reported). One possible explanation for this is that Anderson is not capable of accelerating arbitrary fixed point iterations. Indeed, it has been shown that it can accelerate linearly converging sequences, that quadratically convergent sequences may worsen their performance and anything in between is still an open problem [21].

Convergence of the Sellier method (all the three variants previously shown) is established when the deformed geometry is sufficiently close to the original one, or when the increments are sufficiently small. The latter can lead to stagnation, which we have observed to happen sometimes with Aitken acceleration. For this, we have set a minimum relaxation of 0.5 that truncates smaller values.

6. NUMERICAL TESTS

We perform the numerical tests in four different geometries:

- (1) A 2D square domain.
- (2) A 3D rectangular geometry, commonly referred to as *slab* in the computational cardiology community, subject to surface and volume loads to validate our solvers.

Algorithm 2 Sellier method with load ramp.

```
1: Input: Initial point  $\mathbf{u}^0$ , relaxation  $\alpha > 0$ , tolerance tol, and maximum iterations maxit
2: Set error = 1,  $\mathbf{k} = 0$ ,  $\mathbf{u}^k = \mathbf{u}^0$ 
3: while  $t < 1$  do
4:   while error > tol and  $\mathbf{k} < \mathbf{maxit}$  do
5:     Compute forward displacement  $\mathbf{d}^k$  at  $t$  in  $\Omega(\mathbf{X}^k)$ 
6:     Compute the incremental displacement  $\boldsymbol{\delta}^k = \mathbf{X}^k + \mathbf{d}^k - \mathbf{X}^0$ 
7:     Deform the geometry with displacement  $-\boldsymbol{\delta}^k$ 
8:     Update error,  $k \leftarrow k + 1$ 
9:   end while
10:   $t \leftarrow t + \Delta t$ 
11: end while
12: return Solution  $\mathbf{d} = \mathbf{d}^k$ 
```

Algorithm 3 Generalized Sellier method with load ramp.

```
1: Input: Initial point  $\mathbf{u}^0$ , relaxation  $\alpha > 0$ , tolerance tol, and maximum iterations maxit
2: Set error = 1,  $\mathbf{k} = 0$ ,  $\mathbf{u}^k = \mathbf{u}^0$ 
3: while  $t \leq 1$  do
4:   while error > tol and  $\mathbf{k} < \mathbf{maxit}$  do
5:     if Do Armijo: then
6:       for  $\ell$  in  $\{1, 1/2, \dots, \ell_{\min}\}$  do
7:         Compute forward displacement  $\mathbf{d}^\ell$  at  $t$  in  $\Omega(\mathbf{X}^k)$ 
8:         Compute increment  $\boldsymbol{\delta}^\ell = \mathbf{X}^\ell + \mathbf{d}^\ell - \mathbf{X}^0$ 
9:         If  $k > 0$ , set  $\alpha^\ell = -\alpha \frac{\langle \boldsymbol{\delta}^{k-1}, \boldsymbol{\delta}^\ell - \boldsymbol{\delta}^{k-1} \rangle}{|\boldsymbol{\delta}^\ell - \boldsymbol{\delta}^{k-1}|^2}$ 
10:        Compute  $\mathbf{X}^\ell = \mathbf{X}^k - \ell \alpha^\ell \boldsymbol{\delta}^\ell$ 
11:        Compute line search error error $_\ell$ 
12:        If  $k = 0$  or error $_\ell < \mathbf{error}$ : break
13:      end for // for  $\ell$ 
14:      Find  $\ell^*$  with minimum error $_\ell$ 
15:      Update displacement  $\mathbf{d}^k = \mathbf{d}^{\ell^*}$  and  $\alpha = \alpha^{\ell^*}$ 
16:    else
17:      Compute forward displacement  $\mathbf{d}^k$  at  $t$  in  $\Omega(\mathbf{X}^K)$ 
18:    end if // Do Armijo
19:    if Do Anderson: then
20:      Compute accelerated solution  $\mathbf{d}^k = AA(\mathbf{d}^k, \dots, \mathbf{d}^{k-m})$ 
21:    end if // Do Anderson
22:    Compute the incremental displacement  $\boldsymbol{\delta}^k = \mathbf{X}^k + \mathbf{d}^k - \mathbf{X}^0$ 
23:    Deform the geometry with displacement  $-\alpha \boldsymbol{\delta}^k$ 
24:    Update error,  $k \leftarrow k + 1$ 
25:  end while
26:   $t \leftarrow t + \Delta t$ 
27: end while
28: return Solution  $\mathbf{d} = \mathbf{d}^k$ 
```

- (3) A simplified left ventricle (LV) geometry subject to an endocardial pressure and an active stress force.
- (4) A realistic full-heart geometry with given physiological values of atrial and ventricular pressures.

The scope of this section is to clarify the following points: (i) to understand whether it is advantageous to solve the IEP using the Cauchy formulation or the Eshelby one, (ii) to compare the performance of IEP by using its direct solution or a Sellier approach in terms of its robustness (behavior with varying parameters) and optimality (sensitivity on problem size), and (iii) to characterize the computational effort of the IEP with respect to the DEP, i.e. which problem is most computationally challenging, and how to measure this aspect. For these aims, the numerical tests we propose are the following.

- (1) A numerical convergence test for the Cauchy and Eshelby formulations for varying degrees of approximation. This test will help us conclude which of the two formulations should be used in practice.
- (2) A robustness test where we vary the load of the slab and the endocardial pressure/active stress of the idealized LV. This test measures the sensitivity of the solvers with respect to external loads.
- (3) An optimality test in which, for fixed loads, we increase the degrees of freedom of each problem. This test measures the sensitivity of the solvers with respect to the problem size.
- (4) A preconditioning test, where we study the performance of both algebraic multigrid (AMG) and domain decomposition (DD) methods for the IEP formulation.
- (5) A formulation comparison test, in which we study whether the backward or forward problems are more computationally demanding.
- (6) A real-case scenario where we can test our conclusions in a full-heart model.

In what follows, we will use the term *inverse displacement method* to denote a direct numerical approximation of the IEP, based either on a finite element approximation of the Cauchy version (26) or the Eshelby one (27). The inverse displacement method is thus a way, alternative to the Sellier's method, to solve the IEP, and should not be confused with the latter.

To avoid ambiguity, we will consider the nonlinear iterations to be the number of iterations required for each method to converge. For the inverse displacement method, this will be the number of Newton iterations. Instead, for the Sellier method, this will refer to the fixed point iterations required for convergence. Given that at each fixed point iteration this method incurs on the solution of a nonlinear elasticity problem, we will refer to such iterations as the inner nonlinear iterations. Whenever more than one ramp step is used, we will report the average number of iterations. The implementation of all tests on the slab and on the idealized LV have been implemented with the FEniCS library [2] and visualized with Paraview [29]. The preconditioning tests have been performed with the Firedrake library [47]. In addition, unless stated otherwise, all linear systems are solved using the MUMPS library [5], which uses a direct method. This avoids the additional complexity of considering the challenges associated with the linear system resolution whenever quantifying the computational burden of the IEP. The real-case scenario was performed with the high-performance c++ library `lifex` (see² and [1]), built upon the finite element core `deal.II` (see³ and [7]).

6.1. Numerical convergence test. In this section, we propose a simple convergence analysis of the discretized counterparts of the weak formulations (26)-(27). We consider the 2D square domain $\Omega = [0, L] \times [0, L]$, and assume that the body is homogeneous and composed of a material with Neo-Hookean strain energy (16). We construct the fields \mathbf{b} and \mathbf{t} such that

$$(32) \quad \hat{\mathbf{u}}(\mathbf{x}) = A \sin(2\pi x_1) \mathbf{e}_2$$

is a solution of the inverse problem. In (32), $\mathbf{x} = x_1 \mathbf{e}_1 + x_2 \mathbf{e}_2$ and $(\mathbf{e}_1, \mathbf{e}_2)$ is the canonical basis in \mathbb{R}^2 .

We can now compute the corresponding Cauchy stress tensor through (17) and, by applying (3) we can recover the corresponding fields \mathbf{b} and \mathbf{t} . Similarly, from (12) we can recover the expressions of $\boldsymbol{\beta}$ and $\boldsymbol{\sigma}$ such that (32) is a solution of (11).

We use this analytical solution to perform the convergence analysis of the discretized problem. We exploit a Galerkin approximation and the finite element method. We construct a triangular, structured mesh Ω_h of the domain Ω , with h being the diagonal of the elements. We use P^1 , P^2 and P^3 elements to discretize the field $\hat{\mathbf{u}}$ and we denote by $\hat{\mathbf{u}}_h$ the discrete counterpart. The nonlinear problem is solved by means of a Newton method.

In Figure 6, we show a logarithmic plot of the error norm $\|\hat{\mathbf{u}} - \hat{\mathbf{u}}_h\|_{H^1(\Omega, \mathbb{R}^2)}$ for $A = 0.1L$. We observe that the error is $O(h^n)$ for the element P^n as $h \rightarrow 0$. The errors measured using the weak forms (26) and (27) are very close, even though the formulation using the Eshelby stress (27) requires much more iterations. Indeed, for the formulation with the Cauchy stress tensor, we can solve the problem with a single Newton algorithm which requires an average of 5.2 inner iterations. Conversely, with the Eshelby stress the direct application of the Newton method may fail and we need to use a ramp where we iteratively increase the value of A , see Table 2. Therefore, in the remaining part of this work, we will focus our attention on the Cauchy stress weak form (26).

²<https://lifex.gitlab.io/>

³<https://www.dealii.org>

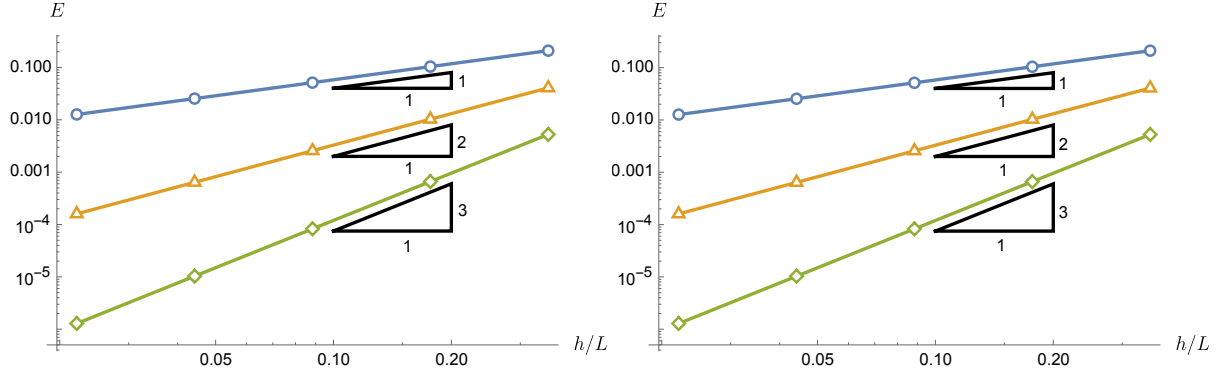


FIGURE 6. Results of the convergence analysis for the problem described in Section 6.1. Here we show E , i.e. the error norm $\|\hat{\mathbf{u}} - \hat{\mathbf{u}}_h\|_{H^1}$ non-dimensionalized with respect to the length-scale L , as a function of h/L for the weak formulations (26) (left) and (27) (right) for $\lambda/\mu = 1000$. The blue, orange, and green markers correspond to the solutions obtained with P^1 , P^2 , and P^3 elements, respectively. The two plots are almost identical and we do not have significant differences in the marker positions.

		<i>Cauchy formulation</i>		<i>Eshelby formulation</i>	
n	Element	Newton iterations	Ramp steps	Newton iterations	
4	P1	5	2	6.5	
8	P1	5	2	7.0	
16	P1	5	2	10.0	
32	P1	5	9	5.3	
64	P1	5	10	5.7	
4	P2	5	3	8.0	
8	P2	5	4	9.0	
16	P2	5	7	7.1	
32	P2	5	11	5.7	
64	P2	6	12	5.7	
4	P3	5	4	7.8	
8	P3	5	10	5.5	
16	P3	5	11	5.6	
32	P3	6	12	5.7	
64	P3	6	13	5.6	

TABLE 2. Average number of Newton iterations per ramp step and ramp steps necessary for solving the problem described in Section 6.1. Here, we use just one ramp step for the Cauchy formulation and n is the number of element for each side of the square domain.

6.2. Slab tests. The slab consists in a prism cut going from the endocardium to the epicardium, given by $\Omega := (0, 10^{-2} \text{ m}) \times (0, 3 \cdot 10^{-3} \text{ m}) \times (0, 3 \cdot 10^{-3} \text{ m})$. On it, we consider the exponential constitutive law of Usyk [62], detailed in Section 6.5, with homogeneous Dirichlet conditions on $\{x = 0\}$ and null traction conditions elsewhere. We display the solution of the inverse displacement problem in Figure 7, which we computed for various volumetric and surface loads, given by \mathbf{b} and \mathbf{t} respectively in (3). We note that both solutions were computed using 10 ramp steps for the loads, and the maximum load used for each display was such that twice bigger loads would yield a divergent iterative procedure using the IEP formulation.

6.2.1. Robustness. We study the robustness with respect to volumetric loads. To measure the performance, we look at the number of nonlinear iterations required for convergence. All tests were performed with a Newton method using absolute and relative tolerances of 10^{-14} and 10^{-6} respectively for the inverse problem. The Sellier methods use equal absolute and relative tolerances of 10^{-6} . The tangent

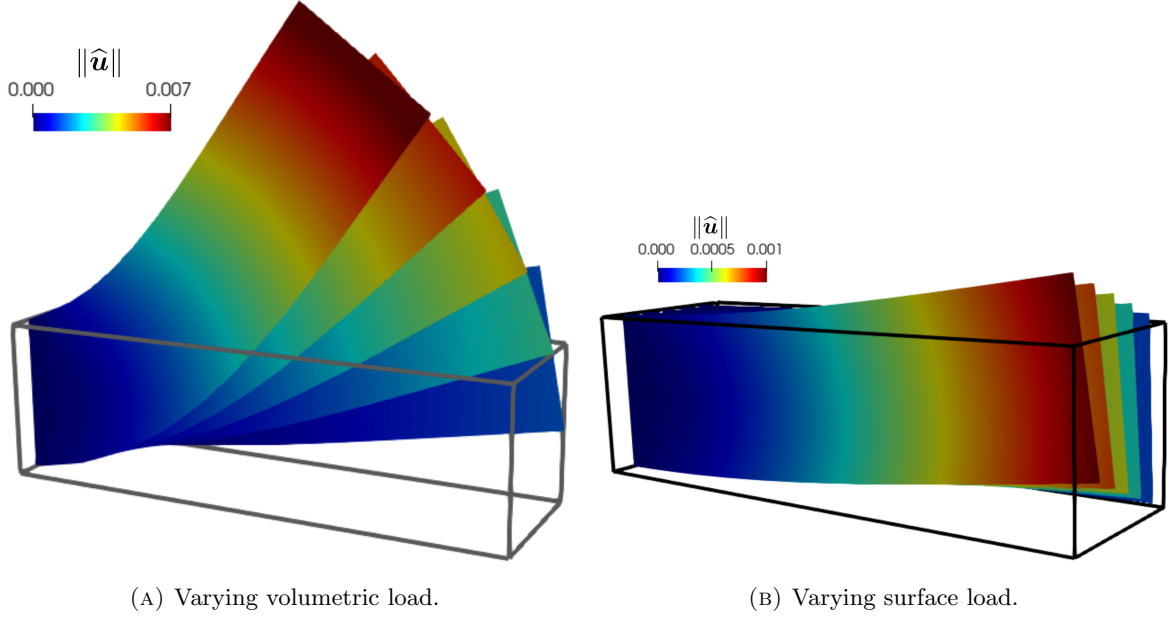


FIGURE 7. Solution of the inverse displacement problem computed on a slab. In Figure (a), we compute the stress-free configuration for forces $\mathbf{b} = -b\hat{\mathbf{e}}_z$ with $b \in \{10 \text{ Pa m}^{-1}, 20 \text{ Pa m}^{-1}, 30 \text{ Pa m}^{-1}, 40 \text{ Pa m}^{-1}, 50 \text{ Pa m}^{-1}\}$ with surface load $\mathbf{t} = \mathbf{0}$. In Figure (b) we do the same for $\mathbf{b} = \mathbf{0}$ and $\mathbf{t} = -t\hat{\mathbf{e}}_z$ with $t \in \{5 \text{ Pa}, 10 \text{ Pa}, 15 \text{ Pa}, 20 \text{ Pa}, 25 \text{ Pa}\}$.

systems were inverted with MUMPS, a parallel direct solver. The geometry was discretized with 24 subdivisions in the x direction, and 8 subdivisions in the y and z directions, resulting in roughly 6 000 degrees of freedom.

We show the results of this test in Table 3. We first note that the inverse displacement method is much more robust than the Sellier methods in general, being able to yield a solution for load values more roughly 10 times larger than those of Sellier methods, in only one ramp step, and 4 times larger if Sellier uses 100 ramp steps. Among Sellier methods, we note that they all converge in the same scenarios, meaning that acceleration does not make a difference in this test. Still, it can be appreciated how the Armijo strategy yields a more robust method, which can be greatly improved by using instead Anderson acceleration. Indeed, the latter can sometimes yield convergence in roughly half the number of nonlinear iterations. Still, the superiority of this strategy is less obvious when looking at the inner nonlinear iterations, which increase as the accelerated methods perform larger steps. Naturally, this nested solver problem is not present in the inverse displacement method.

6.2.2. Optimality. In this section, we study the sensitivity of the slab problem as the number of degrees of freedom increases. For this, we consider two volumetric loads given by $\mathbf{b} = -b\mathbf{e}_3$ for b in $\{10 \text{ Pa m}^{-1}, 20 \text{ Pa m}^{-1}\}$, and we divide the x , y , and z axes into $3k$, k , and k elements respectively, for k in $\{2, 4, 8, 16, 24, 32, 40\}$, solved in one ramp step. We show the results in Table 4, where we highlight the following results: (i) as is typical of Newton methods, the IEP formulation behaves optimally, with its number of nonlinear iterations remaining constant as the number of degrees of freedom increase [33]. (ii) For the smaller load test, the pure Sellier and its Armijo variant are vastly more reliable than the Anderson accelerated variant. Still, for larger loads they all behave very erratically, and there is no obvious better option.

6.2.3. Performance comparison. In this section we compare the CPU times (also referred to as walltime) of the methods under consideration. For this, we present them for the first scenario considered in the optimality test, i.e. for the load $\mathbf{b} = -10 \text{ Pa m}^{-1}\mathbf{e}_3$, and report them in Table 5. We note that the inverse displacement method provides a clear improvement over the Sellier method, representing roughly a speed-up of an 87%. We highlight that, whenever the Anderson method converges, it is faster than both Sellier variants present in literature. Additionally, we confirm the overall superiority of the Armijo line search strategy for this case, as it is both more robust and faster than plain Sellier.

Vol load	ID			Sellier		
	1	10	100	1	10	100
1	3	2	2	2.0 (2.3)	1.0 (2.0)	1.0 (1.9)
10	4	3	2	8.0 (3.3)	3.7 (2.5)	2.0 (2.0)
25	5	3	3	–	17.0 (3.0)	8.0 (2.5)
50	6	4	3	–	–	–
75	7	4	3	–	–	–
100	–	4.1	3	–	–	–

Vol load	Sellier Armijo			Sellier Anderson		
	1	10	100	1	10	100
1	2.0 (2.3)	1.0 (2.0)	1.0 (1.9)	2.0 (2.3)	1.0 (2.0)	1.0 (1.9)
10	9.0 (3.2)	3.9 (2.5)	2.0 (2.0)	4.0 (4.0)	3.2 (2.5)	2.0 (2.0)
25	–	12.0 (4.5)	6.5 (3.6)	–	4.7 (3.2)	3.5 (2.6)
50	–	–	–	–	–	–
75	–	–	–	–	–	–
100	–	–	–	–	–	–

TABLE 3. Slab robustness. Average number of nonlinear iterations (average inner nonlinear iterations in parenthesis) when increasing the volumetric load with 1 ramp step, 10 ramp steps and 100 ramp steps. ID: Inverse displacement, and Anderson acceleration is used with a depth of 3.

N	DoFs	ID	Sellier	Sellier Armijo	Sellier Anderson
2	189	4.0	5.0 (3.0)	5.0 (3.0)	3.0 (3.5)
4	975	4.0	6.0 (3.1)	7.0 (2.9)	4.0 (3.4)
8	6075	4.0	8.0 (3.3)	9.0 (3.2)	4.0 (4.0)
16	42483	4.0	8.0 (3.2)	9.0 (3.2)	–
24	136875	4.0	8.0 (3.2)	9.0 (3.1)	4.0 (4.8)
32	316899	4.0	8.0 (3.2)	9.0 (3.2)	–
40	610203	4.0	7.0 (3.4)	8.0 (3.3)	–

(A) Results with $\mathbf{b} = -10\mathbf{e}_3$.

N	DoFs	ID	Sellier	Sellier Armijo	Sellier Anderson
2	189	4.0	–	10.0 (3.1)	5.0 (3.8)
4	975	4.0	17.0 (3.6)	–	7.0 (3.5)
8	6075	5.0	–	–	8.0 (4.9)
16	42483	5.0	31.0 (3.8)	25.0 (5.9)	–
24	136875	5.0	–	–	–
32	316899	5.0	–	–	–
40	610203	5.0	–	–	–

(B) Results with $\mathbf{b} = -20\mathbf{e}_3$.

TABLE 4. Slab optimality. Average number of nonlinear iterations (and inner nonlinear iterations) when increasing the number of degrees of freedom. (DoFs) Degrees of freedom, (ID) inverse displacement.

6.2.4. *Computational effort of IEP and DEP.* For measuring which formulation is the most challenging at the numerical level, we use as an indicator the number of nonlinear iterations incurred by the nonlinear solver, if it converges. We do so in three scenarios: (i) the IEP formulation (26), (ii) the DEP formulation from the stress-free configuration (25), and (iii) the DEP from the current configuration (25). The distinction between the last two is important because they represent two conceptually different scenarios. In scenario (ii), we compare the inverse and forward problems in a physically consistent setting. In problem (iii), the scope is purely methodological, as we compare the computational effort of the inverse problem with respect to what is done by the Sellier method. As a matter of fact, the fixed-point iterations of the Sellier method envisage a sequence of DEPs, moving from (iii) to (ii). This should provide further

DoFs	ID	Sellier	Sellier Armijo	Sellier Anderson
189	0.03	0.08	0.08	0.05
975	0.06	0.30	0.31	0.20
6075	0.45	3.20	3.37	1.82
42483	8.37	63.89	70.20	—
136875	60.36	398.87	422.18	281.60
316899	248.85	1636.14	1720.43	—
610203	735.73	5844.36	5275.55	—

TABLE 5. Slab performance. Total CPU time employed to solve the problem for each method under consideration. (DoFs) Degrees of freedom, (ID) inverse displacement.

Vol load	ID	ID-forw	Forward
1	2.0	2.0	2.0
10	3.0	3.0	3.0
25	3.0	3.9	3.9
50	4.0	4.0	4.0
75	4.0	4.9	4.0
100	4.1	—	4.3

TABLE 6. Computational effort study. The numbers stand for the average number of nonlinear iterations incurred by the Newton solver. (ID) Inverse displacement problem, (ID-forw) Forward problem from stress-free configuration, and (Forward) is the forward problem from the current configuration.

evidence for the lack of convergence of the Sellier method, justified additionally by the requirement of solving a challenging nonlinear problem at each iteration. We fix the load to be $\mathbf{b} = -10 \text{ Pa m}^{-1} \mathbf{e}_3$.

We show the results in Table 6. Albeit unintuitive, we note that the easiest problem is the inverse one, which has a consistently lower number of nonlinear iterations than the other two problems. Interestingly, the forward problem from the stress-free configuration in this problem is slightly harder than the one posed on the current geometry. We remark that, in this test case, we only focus on the nonlinear solver, and we disregard the challenges associated with the inner linear systems, as we are employing a direct linear solver. This aspect will be addressed later in Sections 6.4 and 6.5.

6.3. Simplified cardiac model. In this section, we study as in Section 6.2 the robustness, optimality, performance, and computational effort of the inverse displacement formulation against standard and accelerated Sellier schemes on an idealized LV geometry. We consider the same physical model as in the slab test, with the only difference of having the physiologically motivated boundary condition of (29) on the epicardium.

We focus on two types of loads, which are the main ones present in cardiac simulations: (i) a pressure acting uniformly on the endocardium and (ii) the active stress, which we depict respectively in Figures 8 and 9 respectively.

6.3.1. Robustness. In this section we study the robustness of the methods with respect to an endocardial pressure going from 0.1 kPa to 10 kPa for 1, 10, and 100 ramp steps. Then, we do the same computation for an active stress magnitude given going from 1 kPa up to 40 kPa.

The computed results are shown in Tables 7 and 8 for the endocardial pressure and the active stress, respectively. First, we note that again the inverse displacement method is the most robust in all scenarios under consideration. There is no significant advantage in augmenting the standard Sellier method with the Armijo strategy, but instead Anderson acceleration provides a consistently more robust solver in both the number of nonlinear iterations and the scenarios in which it converges. We also highlight that the inverse displacement formulation and the Anderson accelerated Sellier method yield the same robustness when using 100 ramp steps.

6.3.2. Optimality. In this section we study the performance of all methods under consideration as the number of degrees of freedom increases. We consider two scenarios: one with a fixed endocardial pressure

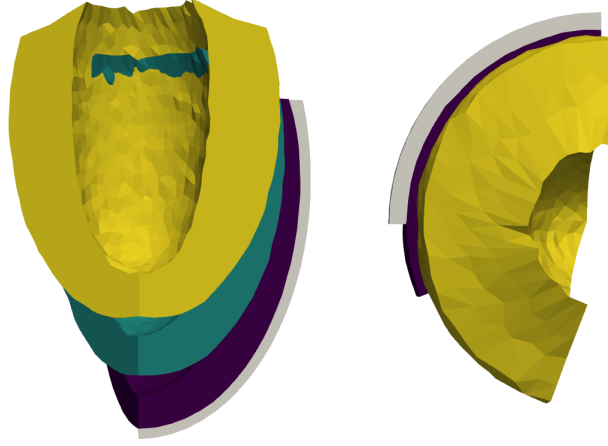


FIGURE 8. Stress-free configuration computed for pressures of 1 kPa (blue), 5 kPa (green), and 10 kPa (yellow).

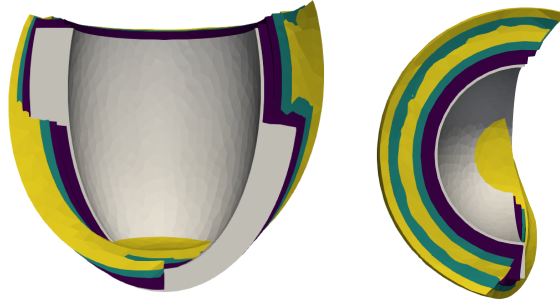


FIGURE 9. Stress-free configuration computed for active stress peaks given by 5 kPa (blue), 10 kPa (green), and 20 kPa (yellow).

Pa	ID			Sellier		
	1	10	100	1	10	100
100	3.0	2.0	2.0	2.0 (2.3)	1.0 (2.0)	1.0 (1.9)
1000	8.0	3.3	2.4	–	7.4 (2.6)	3.7 (2.1)
2500	–	4.2	3.0	–	13.1 (2.7)	6.5 (2.3)
5000	–	4.5	3.0	–	–	6.8 (2.3)
10000	–	–	3.0	–	–	–

Pa	Sellier Armijo			Sellier Anderson		
	1	10	100	1	10	100
100	2.0 (2.3)	1.0 (2.0)	1.0 (1.9)	2.0 (2.3)	1.0 (2.0)	1.0 (1.9)
1000	–	7.2 (2.6)	3.6 (2.2)	–	4.4 (2.7)	2.9 (2.2)
2500	–	10.9 (2.8)	6.5 (2.4)	–	7.6 (2.8)	4.8 (2.4)
5000	–	–	6.7 (2.9)	–	–	5.6 (2.3)
10000	–	–	–	–	–	6.6 (2.4)

TABLE 7. Left ventricle robustness with respect to endocardial pressures. Average number of nonlinear iterations (average inner nonlinear iterations in parenthesis) when increasing the volumetric load with 1, 10, and 100 ramp steps. (ID) Inverse displacement, and Anderson acceleration is used with a depth of 3.

of 0.2 kPa and another one with a fixed active stress peak of 5 kPa, with the results in Table 9. We note that in all considered scenarios, the inverse displacement method yields a more robust performance. Still, we highlight that Anderson acceleration performs roughly the same average inner nonlinear iterations as

Pa	ID			Sellier		
	1	10	100	1	10	100
1000	4.0	3.0	2.0	3.0 (3.0)	1.9 (2.3)	1.0 (2.0)
5000	–	3.2	2.5	–	5.1 (2.6)	2.9 (2.1)
10000	–	3.4	2.6	–	11.8 (2.6)	6.4 (2.1)
20000	–	3.8	2.7	–	–	–
40000	–	–	2.7	–	–	–

Pa	Sellier Armijo			Sellier Anderson		
	1	10	100	1	10	100
1000	4.0 (2.8)	1.9 (2.3)	1.0 (2.0)	3.0 (3.0)	1.9 (2.3)	1.0 (2.0)
5000	–	6.3 (3.8)	3.6 (2.8)	–	4.1 (2.6)	2.7 (2.2)
10000	–	6.9 (3.9)	4.4 (3.1)	–	5.5 (2.7)	3.6 (2.2)
20000	–	–	–	–	–	4.6 (2.4)
40000	–	–	–	–	–	4.9 (2.4)

TABLE 8. Left ventricle robustness with respect to the peak active stress. Average number of nonlinear iterations (average inner nonlinear iterations in parenthesis) when increasing the volumetric load with 1, 10, and 100 ramp steps. (ID) Inverse displacement, and Anderson acceleration is used with a depth of 3.

DoFs	ID	Sellier	Sellier Armijo	Sellier Anderson
9375	3.0	1.4 (2.0)	1.4 (2.0)	1.4 (2.0)
20709	3.0	1.3 (2.0)	1.3 (2.0)	1.3 (2.0)
60081	3.0	1.1 (2.5)	1.1 (2.5)	1.1 (2.5)
149511	3.1	2.2 (2.6)	2.0 (3.0)	1.9 (2.6)

(A) Endocardial pressure of 0.2 kPa.

DoFs	ID	Sellier	Sellier Armijo	Sellier Anderson
9375	3.4	5.1 (2.6)	6.3 (3.8)	4.1 (2.6)
20709	3.4	4.5 (2.7)	5.7 (3.6)	4.0 (2.7)
60081	3.4	5.5 (2.8)	–	4.0 (2.9)
149511	3.6	4.6 (3.1)	5.9 (4.6)	3.9 (3.2)

(B) Peak active stress of 5 kPa.

TABLE 9. LV optimality. We show the average nonlinear iterations (and average inner nonlinear iterations) in ten ramp steps, with an endocardial pressure of 0.2 kPa.

pure Sellier, with reduced nonlinear iterations. In the active stress case, the Armijo strategy is instead both more costly and less robust. Still, there is no significant difference among the methods tested.

6.3.3. Performance comparison. In this section, we compare the CPU times and report them in Table 10. In terms of execution time, we note that pure Sellier is the worst, and inverse displacement yields the best performance, yielding roughly a 60% reduction in time with respect to pure Sellier. Between the two methods reside the Armijo and Anderson accelerated Sellier methods, which yield roughly a 7% and a 10% walltime reduction with respect to a pure Sellier method in the endocardial test. In the active stress case, Sellier Armijo is more expensive, whereas Anderson yields again a 10% time save.

6.3.4. Computational effort of the problem. In this section, we aim to study whether the inverse or forward problems are more computationally demanding as is Section 6.2.4 by considering the same three scenarios. In this case, as in the previous sections, we consider separately the effect of an endocardial pressure and that of an active stress force, shown in Table 11. We note that, as in the slab tests, the inverse displacement method requires the lowest number of iterations in almost all scenarios, except for some instances of active stress. Interestingly, in contrast to the slab case, this test shows that the forward problem from the computed stress-free configuration is easier than the one posed on the deformed configuration for all values considered. This is consistent with experience in cardiac modeling, and shows two things: on one hand, solving the problem from a stress-free configuration is easier, as it

DoFs	ID	Sellier	Sellier Armijo	Sellier Anderson
9375	18.0	30.2	30.4	29.3
20709	52.8	83.1	85.8	86.1
60081	152.3	261.3	264.6	267.6
149511	540.4	1412.6	1325.1	1280.3

(A) Endocardial pressure.

DoFs	ID	Sellier	Sellier Armijo	Sellier Anderson
9375	19.0	93.9	106.3	79.8
20709	57.5	277.4	294.7	251.1
60081	170.8	930.1	–	728.5
149511	618.0	3005.0	3623.4	2697.3

(B) Peak active stress.

TABLE 10. LV CPU times in seconds. (DoFs) Degrees of freedom, (ID) inverse displacement, and Anderson acceleration was used with a depth of 3.

Pa	ID	ID-forw	Forward
100	2.0	2.0	2.0
1000	3.3	3.5	3.7
2500	4.2	4.3	4.7
5000	4.5	–	–

(A) Varying endocardial pressure.

Pa	ID	ID-forw	Forward
1000	3.0	3.0	3.0
5000	3.2	3.0	3.7
10000	3.4	3.4	3.8
20000	3.8	3.6	3.9

(B) Varying active stress.

TABLE 11. Computational effort study on LV. (ID) Inverse displacement problem, (ID-forw) Forward problem from stress-free configuration, and (Forward) is the forward problem from the current configuration.

is more physically accurate for the given geometry. On the other hand, it shows why it is more difficult to get the Sellier method to converge. This suggest that the Sellier method could be made more robust by adding further ramping strategies to the inner nonlinear problem, which would result in even larger computational costs.

6.4. Preconditioning. The main strategy so far to compute preconditioners for nonlinear elasticity has been to devise optimal preconditioners for the linearized formulation, and then use such techniques for the nonlinear scenario. This usually yields satisfactory results in the nonlinear regime, but in this section we show that this approach is not equally valid for the inverse displacement problem. For this, consider the slab problem shown in Section 6.2 with a volumetric load given by $\mathbf{b} = -32 \text{ Pa m}^{-1} \mathbf{e}_3$, which we have observed to be sufficiently large to challenge the numerical solvers. In contrast to all previous numerical tests, where we have used a direct solver (MUMPS) for all linear systems, we display the average number of GMRES iterations using the well-established Algebraic Multigrid implementation from HYPRE [22] for an increasing number of degrees of freedom. This solver is an excellent choice for nonlinear elasticity, and its efficiency has been thoroughly studied for cardiac elasticity as well [11].

We compare its performance with a very simple one-level Additive Schwartz preconditioner with minimal overlap and an incomplete LU (ILU) factorization as a local solver, and show the performance with 16 subdomains (16 MPI processes) in Table 12. We see that, surprisingly, AMG is particularly not suitable for this problem, and an AS/ILU preconditioner provides a better alternative. Moreover, we test the GDSW preconditioner [19] available in PETSc [8] under the same conditions. We provide the results in Table 12, where a much improved performance is obtained in terms of linear iterations, albeit not optimal. We report the PETSc options to use these preconditioners in A. We note that none of the tested preconditioners are optimal, and that obtaining an optimal preconditioner, at least in practice, for the inverse displacement formulation is beyond the scope of this work.

6.5. Realistic four-chamber heart. We now turn to the case of a realistic full-heart model, introduced in Section 3.2. We consider the Zygote Solid 3D Heart Model [63], an anatomically accurate CAD model

DoFs	AMG	AS	GDSW
975	30	62	14
6075	55	118	18
42483	101	287	29
316889	–	1418	53
2446275	–	–	100

TABLE 12. Average number of GMRES iterations incurred in one ramp step by each of the preconditioners considered: (AMG) Algebraic Multigrid, (AS) Additive Schwartz with ILU on 8 sub-domains, and (GDSW) Generalized Driya-Smith-Widlund. Here, “–” denotes a solver that diverged as it attained 5000 linear iterations in one of the Newton steps.

of the whole human heart, obtained from high-resolution CT scans and representing an average healthy male subject, displayed in Figure 10a. We consider a computational mesh with an average cell diameter of 1.18 mm and accounting for $2.75 \cdot 10^6$ tetrahedra (see Figure 10b), generated relying on the algorithms proposed in [24], implemented in the open source software `vmrk` [6].

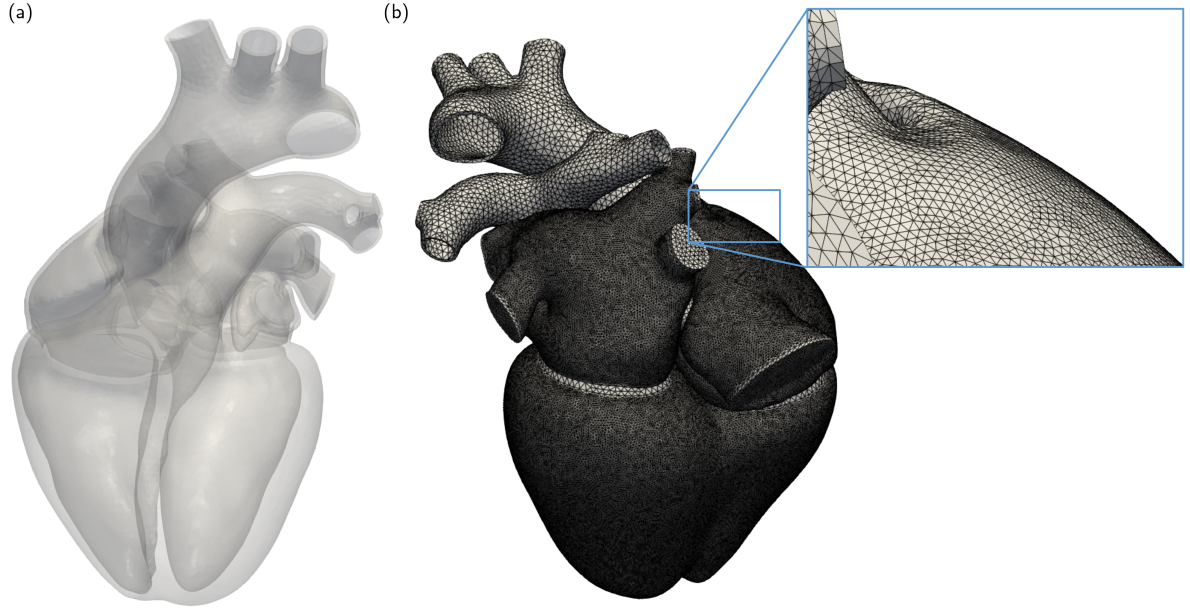


FIGURE 10. Full heart model: (a) computational domain and (b) computational mesh. The mesh is finer in the conductive regions of the myocardium.

We generate the fiber architecture by relying on the Laplace-Dirichlet rule-based method for whole heart geometries proposed in [46] and further refined in [23]. In the myocardium, we consider the exponential constitutive law of Usyk [62], with a volumetric term enforcing quasi-incompressibility:

$$\Psi(\mathbf{F}) = \frac{C}{2} (e^Q - 1) + \frac{B}{2} (J - 1) \log(J)$$

where C is the material stiffness, B is the bulk modulus, and

$$Q = b_{ff} E_{ff}^2 + b_{ss} E_{ss}^2 + b_{nn} E_{nn}^2 + b_{fs} (E_{fs}^2 + E_{sf}^2) + b_{fn} (E_{fn}^2 + E_{nf}^2) + b_{sn} (E_{sn}^2 + E_{ns}^2),$$

$$E_{ab} = \mathbf{E} \mathbf{e}_a \cdot \mathbf{e}_b, \quad \text{for } a, b \in \{f, s, n\},$$

where $\mathbf{E} = \frac{1}{2} (\mathbf{C} - \mathbf{I})$ is the Green-Lagrange strain energy tensor, being $\mathbf{C} = \mathbf{F}^T \mathbf{F}$ the right Cauchy-Green deformation tensor. See the aforementioned reference for the parameter values. In the vessels, instead, we use the Neo-Hookean model:

$$\Psi(\mathbf{F}) = \frac{\mu}{2} \left(J^{-\frac{2}{3}} \text{tr}(\mathbf{F}^T \mathbf{F}) - 3 \right) + \frac{\kappa}{4} \left[(J - 1)^2 + \log^2(J) \right].$$

Left ventricle pressure	13.1 mmHg
Right ventricle pressure	6.0 mmHg
Left atrium pressure	9.0 mmHg
Right atrium pressure	5.6 mmHg
Ascending aorta pressure	71.2 mmHg
Pulmonary trunk pressure	12.8 mmHg
Active tension	7.5 kPa

TABLE 13. Load values considered in the full-heart test case.

We employ the parameters values reported in [23]. We consider a factor $\alpha_n = 0.4$ to account for the effect of microscale fiber dispersion on the active stress. Concerning the epicardium boundary conditions, we set $K_t = 0$ and $K_n = 2 \cdot 10^5 \text{ Pa m}^{-1}$.

To define the IEP, we consider the pressures and diastolic tension reported in Table 13. We consider two load cases, namely 50% and 100% of the values reported in Table 13.

In this test case, we consider both the IEP (that we address with the inverse displacement method and with the Sellier method), and the DEP after having computed the stress-free configuration. Both problems are considerably challenging, due to the highly-nonlinear constitutive law and to the nontrivial geometric features of the considered domain. As a matter of fact, none of the solution methods considered is able to reach convergence with a single load step. Hence, we consider a load-ramp approach by increasing simultaneously both the cavity pressures and the active tension. In such a challenging problem, as the ramp approaches the target value, smaller and smaller steps are typically required to avoid convergence failures, especially when the Sellier method is considered [51]. Hence, to avoid the need of manually tuning the ramp step, we implement the adaptive ramp algorithm of [51], by which the ramp step size is automatically decreased (by a factor 0.7) in case of failure, while it is increased (by a factor 1.2, with a maximum of 0.2 relative step length) in case of success.

The considered problem is challenging also because of the ill-conditioning of the linear systems arising from each Newton iteration. Hence, in order to mitigate the computational burden, we consider, besides the standard Newton algorithm, an Inexact Newton algorithm that employs a loose tolerance for the linear solver in the first nonlinear solver iteration, and progressively reduces it during the iterations. This strategy has been shown to reduce CPU times in cardiac simulations [10] without sacrificing robustness nor optimality. Moreover, we employ the GMRES method by setting a large maximum number of iterations (namely 10^4). We consider both an algebraic multigrid (AMG) preconditioner, and an additive Schwarz method with an ILU approximate solve as inner solver, based on the parallel partitioning (AS/ILU) as shown in Section 6.4. For linear algebra operations we rely on the Trilinos library [60]. Simulations are run on a parallel computing cluster on 92 cores (Lenovo SR950 192-Core Intel Xeon Platinum 8160, 2100 MHz and 1.7TB RAM) at MOX, Department of Mathematics, Politecnico di Milano.

We report in Table 14 the results in terms of convergence success, wall time, number of iterations. First, we notice that the Inexact Newton approach brings in all the considered cases a significant advantage (between 2x and 8x speedup).

Instead, the two considered preconditioners behave very differently depending on the differential problem being solved (namely (25) or (26)). As shown in Section 6.4, AMG shows to be ineffective for the IEP, since the maximum number of GMRES iterations is very often reached, despite the fact that the adaptive algorithm leads to smaller and smaller steps in the ramps. Instead, the AS/ILU method provides a more robust preconditioner for this problem. In contrast, when we consider the DEP or the Sellier method for the IEP (which, at each step, solves a DEP), the choice of preconditioner does not determine the ability to reach convergence or not, but it impacts the wall time. Comparing the results obtained with AMG and AS/ILU, we see that the number of Newton steps is virtually identical, but the wall time is roughly half using AMG. The only exception is in the case of the Sellier method with the traditional Newton algorithm, for which using AS/ILU the nonlinear solver performs about 50% more iterations, meaning that GMRES fails more often than with AMG. In any case, for solving the DEP (25), AMG proves preferable to AS/ILU.

Finally, we compare the inverse displacement method with the Sellier method in solving the IEP. We observe that the Sellier method is unable to reach convergence in this real-life test case when 100% of the load is considered, regardless the nonlinear and linear solvers employed. When we consider a 50% reduction of the load, both methods converge, but the inverse displacement method is remarkably more

Problem	Nonlinear solv.	Linear solv.	50% load				100% load			
			Wall time	F.P. steps	Newt. steps	Time per step	Wall time	F.P. steps	Newt. steps	Time per step
ID	Newton	AMG	> 24h				> 24h			
ID	Inexact Newton	AMG	> 24h				> 24h			
ID	Newton	AS/ILU	36m 20s		21	103.8s	64m 20s		43	89.8s
ID	Inexact Newton	AS/ILU	12m 01s		25	28.8s	19m 30s		38	30.8s
Sellier	Newton	AMG	331m 41s	82	295	67.5s	> 24h			
Sellier	Inexact Newton	AMG	41m 00s	42	160	15.4s	> 24h			
Sellier	Newton	AS/ILU	568m 20s	108	364	93.7s	> 24h			
Sellier	Inexact Newton	AS/ILU	77m 32s	42	166	28.1s	> 24h			
ID-forw	Newton	AMG	20m 31s		27	45.6s	32m 02s		40	48.0s
ID-forw	Inexact Newton	AMG	7m 10s		25	17.2s	13m 51s		41	20.3s
ID-forw	Newton	AS/ILU	42m 50s		27	95.2s	40m 50s		40	61.3s
ID-forw	Inexact Newton	AS/ILU	14m 06s		26	32.5s	20m 04s		42	28.6s

TABLE 14. Results of the realistic 4 chamber cardiac model of Section 6.5. We report: the wall time; the number of fixed point steps (only for the Sellier method); the total number of Newton steps (summed over the ramp steps and, for the Sellier method, over the fixed point iterations); The wall time per each Newton step.

efficient (12 minutes against 41 minutes in the best case, that is with AS/ILU and AMG, respectively). The inverse displacement requires the resolution of more demanding linear systems (28.8s against 15.4s), but this is compensated by a significantly smaller number of Newton steps (25 against 160).

We conclude this section by showing the results obtained in the real-life full heart model. In Figure 11 we show the magnitude of the displacement from the stress-free configuration and the deformed one. In Figure 12 we report several views of the deformed and the stress-free configuration. As expected, the cardiac chambers are deflated, because of the pressures acting on the endocardium. In addition, the chambers that are deformed the most are those with a thinner wall, since they are more prone to being stretched by pressure, and thus the stress-free configuration is more distant from the deformed one. Atria are deflated to a remarkable degree, an aspect that makes calculating the stress-free configuration particularly challenging in this test case. Such deflation induces a rotation in the right atrium auricle, so that a self-penetration of the domain occurs, both of the atrium into the ventricle and of the opposite walls of the atrium. The self-penetration of the relaxed configuration is the manifestation of a global geometric incompatibility, as discussed in Section 2.3.

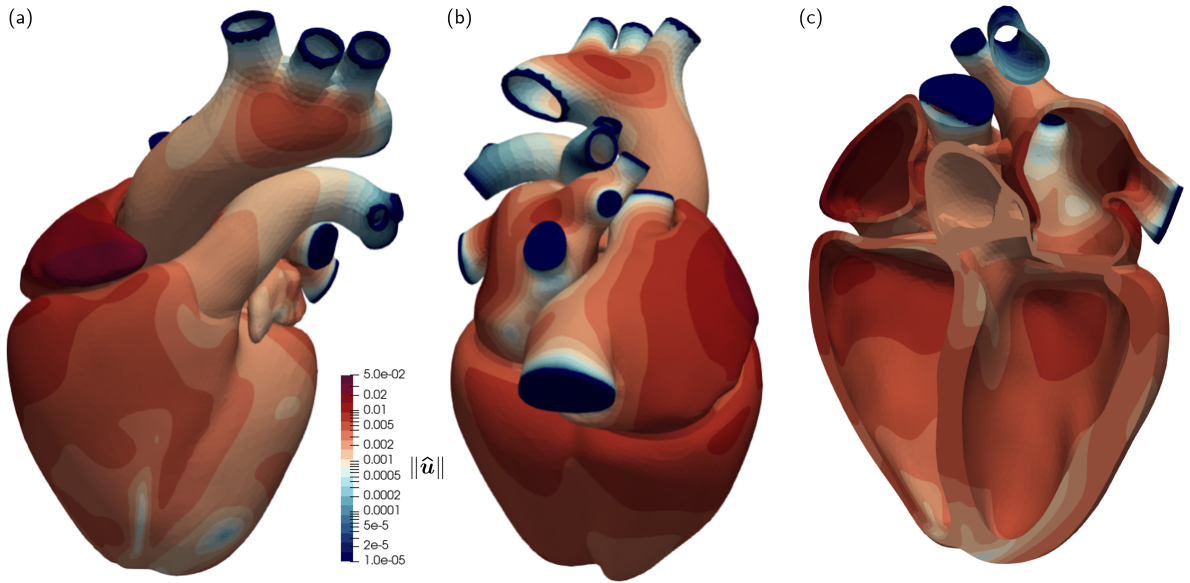


FIGURE 11. Inverse displacement magnitude in the full heart test case. We report: (a) a frontal view; (b) a top view showing the atria; (c) a section, showing the endocardium.

7. CONCLUSIONS

In this paper, we have delved into the complex task of reconstructing the stress-free configuration of an elastic body, terming this challenge the *inverse elasticity problem*.

In Section 2, we have demonstrated that obtaining the inverse deformation map involves solving a mixed boundary value problem that shares structural similarities with the classical problem of hyperelasticity. Expanding upon Shield's pioneering findings [57], we have extended our analysis to encompass the impact of material inhomogeneities, body and active forces.

Although our investigation has revealed that the existence of solutions can be ensured under stringent assumptions, we have uncovered that, even for a simple scenario involving a two-dimensional disk composed of Neo-Hookean material and subjected to external pressure, the problem can yield one, multiple, or even zero solutions depending on the applied pressure.

Furthermore, we have conducted an analysis of potential global geometric incompatibilities, leading to a non-injective inverse deformation. While injectivity of the deformation is pivotal in the direct problem to avoid self-intersections, we have shown that this characteristic is not mandatory for the inverse deformation, and characterized numerically two different mechanisms in which this phenomenon can arise. Nevertheless, the resulting self-intersecting relaxed state of the body could pose issues, rendering the domain unsuitable as a reference configuration. To counteract this challenge, we have proposed

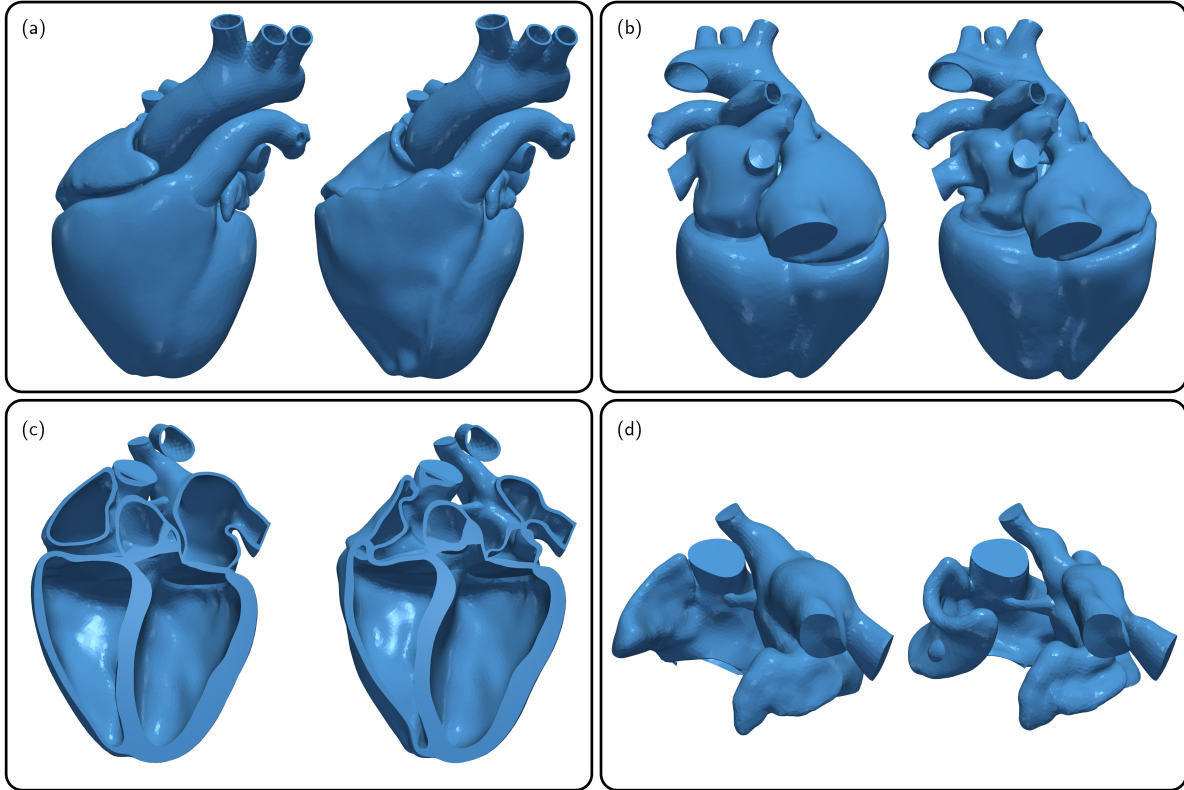


FIGURE 12. Original domain (left) and stress-free configuration (right) in the full heart test case. We show: (a) a frontal view; (b) a top view; (c) a section, showing the endocardium; (d) a section, showing the atria.

a novel approach outlined in Section 2.3, based on a multiplicative decomposition of the deformation gradient tensor.

We have then thoroughly studied the inverse displacement method in terms of its numerical behavior, both independently and in comparison to alternative fixed-point (Sellier) algorithms. Our numerical evidence suggests that

- (i) the inverse displacement method outperforms the Sellier methods in terms of convergence speed and robustness,
- (ii) the Sellier algorithm can be slightly enhanced with Anderson acceleration, but the advantage is negligible when compared against using the inverse displacement method,
- (iii) the inverse displacement problem can be equivalently formulated in terms of the Cauchy and Eshelby stress tensors, but using the Cauchy formulation requires a smaller computational effort,
- (iv) in terms of nonlinear solvers, the inverse displacement problem behaves similarly to the standard elasticity problem, and
- (v) preconditioning the inverse displacement problem is significantly more challenging, and we have shown that domain decomposition preconditioners are significantly more effective than AMG.

We have challenged both the inverse displacement method and the Sellier method in a real-life full heart test case, characterized by detailed anatomical features and by a computational mesh having $2.75 \cdot 10^6$ tetrahedra. The most striking result in this test case is the higher robustness and better performance of the inverse displacement method compared to the Sellier method, the latter being the only one being used at present – to our knowledge – in the cardiac modeling community. As a matter of fact, by relying on the inverse displacement method we were able to recover the stress-free configuration for a realistic load. To the best of our knowledge, this is the first result of this kind in the scientific literature, for a geometry of comparable complexity. Remarkably, the computation took only 19m 30s on 92 cores, that is only 40% more than solving the direct elasticity problem on the same mesh for the same load.

```

"snes_type": "newtonls",
"snes_atol": 1e-12,
"snes_rtol": 1e-6,
"snes_stol": 0.0,
"snes_linesearch_type": "basic",
"ksp_type": "gmres",
"ksp_atol": 0.0,
"ksp_rtol": 1e-6,
"ksp_max_it": 5000,
"ksp_norm_type": "unpreconditioned",
"ksp_gmres_restart": 1000,
"pc_type": "hypre"

```

LISTING 3. PETSc commands to use AMG.

```

"snes_type": "newtonls",
"snes_atol": 1e-12,
"snes_rtol": 1e-6,
"snes_stol": 0.0,
"snes_linesearch_type": "basic",
"ksp_type": "gmres",
"ksp_atol": 0.0,
"ksp_rtol": 1e-6,
"ksp_max_it": 5000,
"ksp_norm_type": "unpreconditioned",
"ksp_gmres_restart": 1000,
"pc_type": "asm",
"sub_ksp_type": "preonly",
"sub_pc_type": "ilu"

```

LISTING 4. PETSc commands to use AS.

```

"snes_type": "newtonls",
"snes_atol": 1e-12,
"snes_rtol": 1e-6,
"snes_stol": 0.0,
"snes_linesearch_type": "basic",
"ksp_type": "gmres",
"ksp_atol": 0.0,
"ksp_rtol": 1e-6,
"ksp_max_it": 5000,
"ksp_norm_type": "unpreconditioned",
"ksp_gmres_restart": 1000,
"pc_type": "mg",
"pc_mg_galerkin": None,
"pc_mg_levels": 2,
"pc_mg_adapt_interp_coarse_space": "gdsw",
"mg_levels_pc_type": "asm"

```

LISTING 5. PETSc commands to use GDSW.

APPENDIX A. PETSC OPTIONS FOR PRECONDITIONERS

In Listings 3-5, we report the PETSc options used to test the preconditioners AMG, ILU, and GDSW in Section 6.4.

ACKNOWLEDGMENT

DR gratefully acknowledges funding by the European Union – NextGenerationEU under the National Recovery and Resilience Plan (NRRP), Mission 4 Component 2 Investment 1.1 - Call PRIN 2022 No. 104 of February 2, 2022 of Italian Ministry of University and Research; Project 202249PF73 (subject area: PE

- Physical Sciences and Engineering) “Mathematical models for viscoelastic biological matter”. NB has been supported by CMM BASAL project FB2100005 and by ANID POSTDOCTORAL 3230325. FR and DR are members of the INdAM research group GNCS (FR) and GNFM (DR). FR and DR acknowledge the support by the MUR, Italian Ministry of University and Research (Italy), grant “Dipartimento di Eccellenza 2023-2027”.

REFERENCES

- [1] P. C. Africa. lifex: A flexible, high performance library for the numerical solution of complex finite element problems. *SoftwareX*, 20:101252, 2022.
- [2] M. Alnæs, J. Blechta, J. Hake, A. Johansson, B. Kehlet, A. Logg, C. Richardson, J. Ring, M. Rognes, and G. Wells. The FEniCS project version 1.5. *Archive of Numerical Software*, 3(100), 2015.
- [3] M. S. Alnæs, A. Logg, K. B. Ølgaard, M. E. Rognes, and G. N. Wells. Unified form language: A domain-specific language for weak formulations of partial differential equations. *ACM Transactions on Mathematical Software*, 40(2):1–37, Feb. 2014.
- [4] D. Ambrosi and S. Pezzuto. Active stress vs. active strain in mechanobiology: Constitutive issues. *Journal of Elasticity*, 107(2):199–212, July 2011.
- [5] P. R. Amestoy, I. S. Duff, J.-Y. L’Excellent, and J. Koster. MUMPS: a general purpose distributed memory sparse solver. In *International Workshop on Applied Parallel Computing*, pages 121–130. Springer, 2000.
- [6] L. Antiga, M. Piccinelli, L. Botti, B. Ene-Iordache, A. Remuzzi, and D. A. Steinman. An image-based modeling framework for patient-specific computational hemodynamics. *Medical & Biological Engineering & Computing*, 46(11), nov 2008.
- [7] D. Arndt, W. Bangerth, T. Clevenger, D. Davydov, M. Fehling, D. Garcia-Sanchez, G. Harper, T. Heister, L. Heltai, M. Kronbichler, R. Kynch, M. Maier, J.-P. Pelteret, B. Turcksin, and D. Wells. The **deal.II** Library, Version 9.1. *Journal of Numerical Mathematics*, 2019.
- [8] S. Balay, S. Abhyankar, M. Adams, J. Brown, P. Brune, K. Buschelman, L. Dalcin, A. Dener, V. Eijkhout, W. Gropp, D. Karpeyev, D. Kaushik, M. Knepley, D. May, L. Curfman McInnes, R. Mills, T. Munson, K. Rupp, P. Sanan, B. Smith, S. Zampini, H. Zhang, and H. Zhang. PETSc users manual. Technical Report ANL-95/11 - Revision 3.13, Argonne National Laboratory, 2021.
- [9] J. Ball. Convexity conditions and existence theorems in nonlinear elasticity. *Archive for Rational Mechanics and Analysis*, 63(4):337–403, 1976.
- [10] N. A. Barnafi, L. F. Pavarino, and S. Scacchi. Parallel inexact newton–krylov and quasi-newton solvers for nonlinear elasticity. *Computer Methods in Applied Mechanics and Engineering*, 400:115557, 2022.
- [11] N. A. Barnafi, L. F. Pavarino, and S. Scacchi. A comparative study of scalable multilevel preconditioners for cardiac mechanics. *Journal of Computational Physics*, 492:112421, 2023.
- [12] J. D. Bayer, R. C. Blake, G. Plank, and N. A. Trayanova. A novel rule-based algorithm for assigning myocardial fiber orientation to computational heart models. *Annals of Biomedical Engineering*, 40:2243–2254, 2012.
- [13] M. Bucelli, L. Dede, A. Quarteroni, and C. Vergara. Partitioned and monolithic algorithms for the numerical solution of cardiac fluid-structure interaction. *Communications in Computational Physics*, 32(5):1217–1256, jun 2022.
- [14] M. M. Carroll. Compressible isotropic strain energies that support universal irrotational finite deformations. *The Quarterly Journal of Mechanics and Applied Mathematics*, 58(4):601–614, 2005.
- [15] M. M. Carroll and F. J. Rooney. Implications of shield’s inverse deformation theorem for compressible finite elasticity. *Zeitschrift für angewandte Mathematik und Physik*, 56(6):1048–1060, nov 2005.
- [16] P. Chadwick. Applications of an energy-momentum tensor in non-linear elastostatics. *Journal of Elasticity*, 5(3-4):249–258, nov 1975.
- [17] G. Deng and F. Galetto. Fast iterative reverse filters using fixed-point acceleration. *Signal, Image and Video Processing*, pages 1–9, 2023.
- [18] A. DiCarlo and S. Quiligotti. Growth and balance. *Mechanics Research Communications*, 29(6):449–456, 2002.
- [19] C. R. Dohrmann, A. Klawonn, and O. B. Widlund. A family of energy minimizing coarse spaces for overlapping schwarz preconditioners. In *Domain Decomposition Methods in Science and Engineering XVII*, pages 247–254. Springer, 2008.
- [20] M. Epstein. Mathematical characterization and identification of remodeling, growth, aging and morphogenesis. *Journal of the Mechanics and Physics of Solids*, 84:72–84, 2015.
- [21] C. Evans, S. Pollock, L. G. Rebholz, and M. Xiao. A proof that anderson acceleration improves the convergence rate in linearly converging fixed-point methods (but not in those converging quadratically). *SIAM Journal on Numerical Analysis*, 58(1):788–810, 2020.
- [22] R. Falgout and U. Yang. hypre: A library of high performance preconditioners. In *International Conference on Computational Science*, pages 632–641. Springer, 2002.
- [23] M. Fedele, R. Piersanti, F. Regazzoni, M. Salvador, P. C. Africa, M. Bucelli, A. Zingaro, A. Quarteroni, et al. A comprehensive and biophysically detailed computational model of the whole human heart electromechanics. *Computer Methods in Applied Mechanics and Engineering*, 410:115983, 2023.
- [24] M. Fedele and A. Quarteroni. Polygonal surface processing and mesh generation tools for the numerical simulation of the cardiac function. *International Journal for Numerical Methods in Biomedical Engineering*, 37(4):e3435, 2021.
- [25] M. W. Gee, C. H. Reeps, H. H. Eckstein, and W. A. Wall. Prestressing in finite deformation abdominal aortic aneurysm simulation. *Journal of Biomechanics*, 42(11):1732–1739, 2009.
- [26] G. Gantesio, A. Musesti, and D. Riccobelli. A comparison between active strain and active stress in transversely isotropic hyperelastic materials. *Journal of Elasticity*, 137(1):63–82, dec 2018.
- [27] A. Gorieli and M. Ben Amar. Differential growth and instability in elastic shells. *Physical Review Letters*, 94(19), May 2005.

- [28] S. Govindjee and P. A. Mihalic. Computational methods for inverse finite elastostatics. *Computer Methods in Applied Mechanics and Engineering*, 136(1-2):47–57, 1996.
- [29] A. Henderson. Paraview guide: A parallel visualization application. *Kitware, Inc., Clifton Park, NY*, 2007.
- [30] C. O. Horgan and J. G. Murphy. Invariance of the equilibrium equations of finite elasticity for compressible materials. *Journal of Elasticity*, 77:187–200, 2004.
- [31] C. O. Horgan and J. G. Murphy. Plane strain bending of cylindrical sectors of admissible compressible hyperelastic materials. *Journal of Elasticity*, 81:129–151, 2005.
- [32] A. M. Katz. *Physiology of the Heart*. Lippincott Williams & Wilkins, 2010.
- [33] C. Kelley and E. W. Sachs. Mesh independence of newton-like methods for infinite dimensional problems. *The Journal of Integral Equations and Applications*, pages 549–573, 1991.
- [34] V. I. Kondaurov and L. V. Nikitin. Finite strains of viscoelastic muscle tissue. *Journal of Applied Mathematics and Mechanics*, 51(3):346–353, 1987.
- [35] E. Kröner. Allgemeine kontinuumstheorie der versetzungen und eigenspannungen. *Archive for Rational Mechanics and Analysis*, 4(1):273–334, 1959.
- [36] E. H. Lee. Elastic-plastic deformation at finite strains. *Journal of Applied Mechanics*, 36(1):1–6, Mar 1969.
- [37] L. Marx, J. A. Niestrawska, M. A. F. Gsell, F. Caforio, G. Plank, and C. M. Augustin. Robust and efficient fixed-point algorithm for the inverse elastostatic problem to identify myocardial passive material parameters and the unloaded reference configuration. *Journal of Computational Physics*, 463:111266, 2022.
- [38] A. Mazier, A. Bilger, A. E. Forte, I. Peterlik, J. S. Hale, and S. P. Bordas. Inverse deformation analysis: an experimental and numerical assessment using the FEniCS Project. *Engineering with Computers*, 38(5):4099–4113, 2022.
- [39] J. Merodio and R. W. Ogden. On the equivalence of strong ellipticity in the material and spatial settings of finite elasticity. *Zeitschrift für Angewandte Mathematik und Physik*, 57(6):1096–1101, aug 2006.
- [40] A. Montanino and A. Pandolfi. On the recovery of the stress-free configuration of the human cornea. *Journal for Modeling in Ophthalmology*, 4:11–33, 2020.
- [41] S. Mora, E. Andò, J.-M. Fromental, T. Phou, and Y. Pomeau. The shape of hanging elastic cylinders. *Soft Matter*, 15(27):5464–5473, 2019.
- [42] S. Mora, T. Phou, J.-M. Fromental, and Y. Pomeau. Gravity driven instability in elastic solid layers. *Physical Review Letters*, 113(17), oct 2014.
- [43] F. Morin, H. Courtecuisse, M. Chabanas, and Y. Payan. Rest shape computation for highly deformable model of brain. *Computer Methods in Biomechanics and Biomedical Engineering*, 18(sup1):2006–2007, sep 2015.
- [44] J. G. Murphy. Inverse radial deformations and cavitation in finite compressible elasticity. *Mathematics and Mechanics of Solids*, 8(6):639–650, 2003.
- [45] M. R. Pfaller, J. M. Hörmann, M. Weigl, A. Nagler, R. Chabiniok, C. Bertoglio, and W. A. Wall. The importance of the pericardium for cardiac biomechanics: from physiology to computational modeling. *Biomechanics and Modeling in Mechanobiology*, 18:503–529, 2019.
- [46] R. Piersanti, P. C. Africa, M. Fedele, C. Vergara, L. Dedè, A. F. Corno, and A. Quarteroni. Modeling cardiac muscle fibers in ventricular and atrial electrophysiology simulations. *Computer Methods in Applied Mechanics and Engineering*, 373:113468, 2021.
- [47] F. Rathgeber, D. Ham, L. Mitchell, M. Lange, F. Luporini, A. McRae, G.-T. Bercea, G. Markall, and P. Kelly. Firedrake: automating the finite element method by composing abstractions. *ACM Transactions on Mathematical Software (TOMS)*, 43(3):1–27, 2016.
- [48] M. K. Rausch, M. Genet, and J. D. Humphrey. An augmented iterative method for identifying a stress-free reference configuration in image-based biomechanical modeling. *Journal of Biomechanics*, 58:227–231, 2017.
- [49] F. Regazzoni, L. Dedè, and A. Quarteroni. Active force generation in cardiac muscle cells: mathematical modeling and numerical simulation of the actin-myosin interaction. *Vietnam Journal of Mathematics*, 49:87–118, 2021.
- [50] F. Regazzoni and A. Quarteroni. An oscillation-free fully partitioned scheme for the numerical modeling of cardiac active mechanics. *Computer Methods in Applied Mechanics and Engineering*, 373:113506, 2021.
- [51] F. Regazzoni, M. Salvador, P. C. Africa, M. Fedele, L. Dedè, and A. Quarteroni. A cardiac electromechanical model coupled with a lumped-parameter model for closed-loop blood circulation. *Journal of Computational Physics*, 457:111083, 2022.
- [52] D. Riccobelli, A. Agosti, and P. Ciarletta. On the existence of elastic minimizers for initially stressed materials. *Philosophical Transactions of the Royal Society A: Mathematical, Physical and Engineering Sciences*, 377(2144):20180074, 2019.
- [53] D. Riccobelli and D. Ambrosi. Activation of a muscle as a mapping of stress–strain curves. *Extreme Mechanics Letters*, 28:37–42, Apr. 2019.
- [54] D. Riccobelli and P. Ciarletta. Rayleigh–Taylor instability in soft elastic layers. *Philosophical Transactions of the Royal Society A: Mathematical, Physical and Engineering Sciences*, 375(2093):20160421, apr 2017.
- [55] E. K. Rodriguez, A. Hoger, and A. D. McCulloch. Stress-dependent finite growth in soft elastic tissues. *Journal of Biomechanics*, 27(4):455–467, 1994.
- [56] M. Sellier. An iterative method for the inverse elasto-static problem. *Journal of Fluids and Structures*, 27(8):1461–1470, 2011.
- [57] R. T. Shield. Inverse deformation results in finite elasticity. *Zeitschrift für Angewandte Mathematik und Physik ZAMP*, 18(4):490–500, jul 1967.
- [58] M. Silhavy. *The Mechanics and Thermodynamics of Continuous Media*. Springer Berlin Heidelberg, 1997.
- [59] L. A. Taber and R. Perucchio. Modeling heart development. *Journal of Elasticity*, 61(1):165–198, 2000.
- [60] T. Trilinos Project Team. *The Trilinos Project Website*, 2020 (accessed May 22, 2020).
- [61] C. Truesdell and W. Noll. *The Non-Linear Field Theories of Mechanics*. Springer Science & Business Media, 2013.

- [62] T. P. Usyk, I. J. LeGrice, and A. D. McCulloch. Computational model of three-dimensional cardiac electromechanics. *Computing and Visualization in Science*, 4(4):249–257, 2002.
- [63] Zygote. Zygote solid 3D male anatomy collection generation II development report. Technical report, 2014.